Northwestern University
Department of Materials Science and Engineering
McCormick School of Engineering and Applied Science
Evanston, IL 60208

Final Report

Department of Energy: Grant No. DE-FG02-02ER45997
Sept. 1, 2002 to Feb. 28, 2006

Alloy Design of Nanoscale Precipitation Strengthened Alloys: Design of a Heat Treatable Aluminum Alloy Useful to 400° C

Principal Investigator
Morris E Fine

Co-Principal Investigators
Gautam Ghosh
Dieter Isheim
Semyon Vaynman

Graduate Students
Keith Knipling
Jefferson Z. Liu

May 6, 2006

Alloy Design of Nanoscale Precipitation Strengthened Alloys: Design of a Heat Treatable Aluminum Alloy Useful to 400° C

Abstract

A creep resistant high temperature Al base alloy made by conventional processing procedures is the subject of this research. The Ni-based superalloys have volume fractions of cubic $L1_2$ phase precipitates near 50 %. This is not attainable with Al base alloys and the approach pursued in this research was to add $L1_2$ structured precipitates to the Al-Ni eutectic alloy, 2.7 at. % Ni – 97.3 at. % Al. The eutectic reaction gives platelets of Al_3Ni (DO_{11} structure) in an almost pure Al matrix. The Al_3Ni platelets give reinforcement strengthening while the $L1_2$ precipitates strengthen the Al alloy matrix. Based on prior research and the extensive research reported here modified cubic $L1_2$ Al_3Zr is a candidate. While cubic Al_3Zr is metastable, the stable phase is tetragonal, only cubic precipitates were observed after 1600 hrs at 425° C and they hardly coarsened at all with time at this temperature. Also addition of Ti retards the cubic to tetragonal transformation; however, a thermodynamically stable precipitate is desired. A very thorough *ab initio* computational investigation was done on the stability of $L1_2$ phases of composition, $(Al,X)_3(Zr,Ti)$ and the possible occurrence of tie lines between a stable $L1_2$ phase and the Al alloy terminal solid solution. Precipitation of cubic $(Al_{(1-x)}Zn_x)_3Zr$ in Al was predicted by these computations and subsequently observed by experiment (TEM).

To test the combined reinforcement–precipitation concept to obtain a creep resistant Al alloy, Zr and Ti were added to the Al-Ni eutectic alloy. Cubic $L1_2$ precipitates did form. The first and only Al-Ni-Zr-Ti alloy tested for creep gave a steady state creep rate at 375° C of 8×10^{-9} under 20MPa stress. The goal is to optimize this alloy and add Zn to achieve a thermodynamically stable precipitate.

Table of Contents

Alloy Design of Nanoscale Precipitation Strengthened Alloys: Design of a Heat Treatable Aluminum Alloy Useful to 400° C

Introduction

The goal of this research was to "design and produce a new castable, heat treatable, nanoscale precipitation strengthened aluminum base alloy having creep resistance at high homologous temperatures, well beyond existing alloys"[1]. By analogy with the Ni-base superalloys we sought suitable cubic $L1_2$ structured precipitates. The GP zones that strengthen Al alloys are all metastable and disappear on heating to 200° C or lower. Cubic $L1_2$ Al_3Zr and Al_3Sc are added to commercial wrought Al alloys for grain refinement and to retard recrystallization but the maximum volume fractions of these precipitates are very small. The Ni-based superalloys have volume fractions of the $L1_2$ phase near 50 %. This is not attainable with Al base alloys and the approach pursued in this research was to add $L1_2$ structure precipitates to an Al base casting alloy. The alloy chosen was the Al-Ni eutectic, 2.7 at. % Ni – 97.3 at. % Al. The eutectic reaction gives platelets of Al_3Ni (DO_{11} structure) and almost pure Al. An alternate to Al_3Sc was sought because it is very expensive and has too high a diffusion rate in Al for creep resistance at high temperatures. Cubic Al_3Zr is metastable (tetragonal $D0_{23}$ is the stable structure) and this is a concern for long time creep resistance.

Two approaches were taken to find suitable $L1_2$ structured precipitates for addition to the Al-Ni eutectic alloy. Since the early work of Raman and Schubert [2] many thermodynamically stable ternary intermetallics of approximate composition $(Al_{67}M_8)_3$(Ti or Zr) have been found where M is a transition metal in the series V to Zn. A thorough computational investigation was made of ternary, quaternary and higher component Al base alloys was made seeking $L1_2$ structured precipitates in Al with M = V to Zn with Ti, Zr and or Hf. The result was the *ab initio* prediction and experimental verification of thermodynamically stable $L1_2$- $(Al,Zn)_3Zr$ precipitates in an Al matrix. The second approach was to investigate cubic $Al_3(Zr,Ti)$ precipitates in Al. Earlier work by Parameswaran *et al* [3] showed that precipitates of cubic $Al_3(Zr,Ti)$ in Al resisted coarsening and did not transform to the tetragonal phase for hundreds of hours at 425° C. Later work by Tsau and Chen [4] extended the time to thousands of hours. The precipitate structure and composition of cubic $Al_3(Zr,Ti)$ precipitates in Al were thoroughly studied by TEM and LEAP tomography followed by creep measurements. The Al-Ni eutectic was selected as the reinforcing alloy because of the Pi's previous experience on developing a series of die casting alloys based on this eutectic [5] and a recent paper by Belov et al [6] reporting precipitation hardening from Al_3Zr in eutectic Al-Ni cast in a graphite mold that was aged at 400 to 450° C.

This report consists of four parts. The first part describes the *ab initio* prediction and experimental verification of thermodynamically stable $L1_2$-$(Al,Zn)_3Zr$ precipitates in an Al matrix. The second part describes calculations, synthesis and properties of $L1_2$ $(Al,Cu_x)_{0.75}(Zr_yTi_z)_{0.25}$ intermetallics. The third part is on the $Al_3(Zr,Ti)$ precipitates in Al. The fourth part deals with the microstructure and creep properties of castable Al-Ni eutectic alloys with $Al_3(Zr,Ti)$ precipitates.

PART 1. Formation of Thermodynamically Stable $L1_2$-$(Al,Zn)_3Zr$ Precipitates in Al Matrix – G . Ghosh and J.Z. Liu

1.A. Computational Research

Our computational research is focused on the phase stability and elastic properties of solid phases relevant to the design of a new precipitation strengthened Al-alloy. Besides zero-temperature phase stability, finite temperature effects due to vibrational entropy contributions in Al_3TM with $L1_2$, DO_{22} and DO_{23} structures and (Al) solid solutions were computed. We have employed comprehensive and efficient computational strategies to predict alloy phase stability in order to facilitate the design of new nanoscale, $L1_2$-precipitate strengthened Al alloys. The computational schemes involve (i) zero-temperature total energy calculations employing electronic density functional theory, (ii) finite temperature phase stability calculations to include vibrational entropy contributions to alloy phase stability within the framework of harmonic phonon theory, and (iii) calculation of elastic constants of $L1_2$, DO_{22} and DO_{23} phases. For the first-principles calculations, we have used Vienna *ab initio* Simulation Package (VASP), the details of which are described elsewhere [7-9]. All calculations were performed employing Ultrasoft Pseudopotentials (USPP) [10] and the Generalized-Gradient Approximation.

Synthesis of bulk $L1_2$ phases in Al-Ti-X (X=V, Cr, Mn, Fe, Co, Ni, Cu, Zn, Nb, Mo, Rh, Pd, Ag, Pt, and Au) systems is well known [11,12]. Among these systems, considerations related to known phase diagrams led to the identification of Al-Zn-TM (TM=Ti,Zr,Hf) systems as candidates for the precipitation of "thermodynamically stable" $L1_2$ phases in an (Al) matrix. In these ternary systems, we sought to stabilize the $L1_2$ phase while destabilizing two other competing structures, DO_{22} and DO_{23}, commonly observed in the Al-TM systems. Accordingly, in the absence of any experimental thermodynamic data of Zn-TM (TM=Ti,Zr,Hf) and Al-Zn-TM intermetallics, we investigated the relative stability of the abovementioned ordered structures by first-principles methods which ultimately facilitate the calculation of relevant multicomponent phase diagrams within the Calphad formalism. Combining available experimental information and the present research objectives, the alloy systems chosen for theoretical phase stability study are Al-TM, Al-Cu-TM and Al-Zn-TM, with TM=Ti,Zr,Hf.

1.A.1. Zero-temperature Phase Stability and Cohesive Properties of Al-TM Intermetallics

We have performed systematic calculations of alloying energetics in Al-TM (TM=Ti,Zr,Hf)) systems, which augment the available calorimetric data for enthalpies of formation in support of the development of accurate multicomponent thermodynamic databases for these technologically interesting systems. Figure 1 plots calculated formation energy (ΔE) as a function of TM content. These and other ancillary results have been discussed in detail elsewhere [13]. The accuracy of our calculations is assessed through comparisons between theoretical results and experimental measurements (where available) for lattice

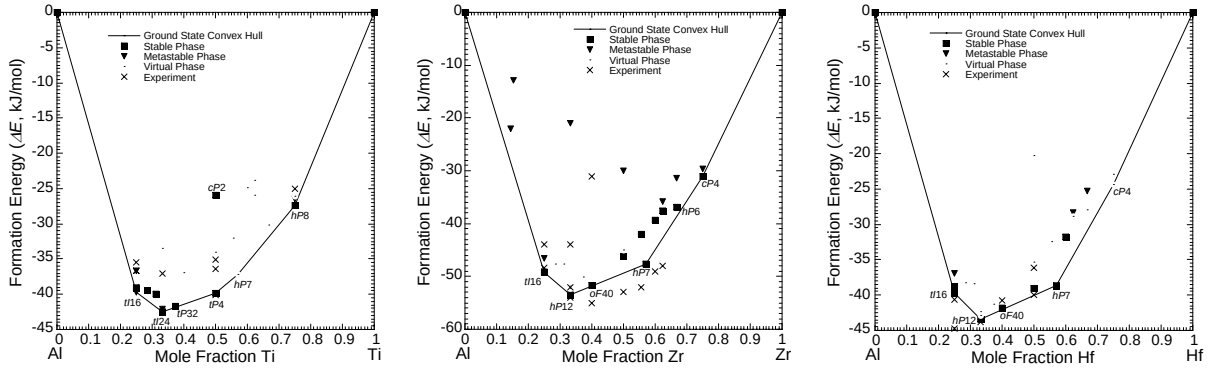

a b c

Figure 1. Calculated zero-temperature formation energy of intermetallics in (a) Al-Ti, (b) Al-Zr and (c) Al-Hf systems. The solid line defines the ground state convex hull [13].

constants, elastic properties and formation energies. The concentration dependencies of the heats of formation for all three binary systems are very similar, being skewed towards the Al-rich side with a minimum around Al_2TM. In all three binary Al-TM systems, the calculated zero-temperature intermetallic formation energies generally agree well, within a few kJ/mole, with calorimetric data obtained by direct reaction synthesis. This level of agreement suggests high accuracy for the calculated enthalpies of formation reported for structures where no such measured data is currently available. Several intermetallic phases, such as Al_3Zr_5 (*hP*16), $AlZr_2$ (*tI*12), Al_3Hf_5(*hP*16) and $AlHf_2$(*tI*12), which have previously been suggested to be stabilized by impurity effects, are indeed found to be higher energy states compared to their stable counterparts. For the stable intermetallics, the calculated zero-temperature lattice parameters agree to within ±1% of experimental data at ambient temperature. For the stable phases with unit cell-internal degree(s) of freedom, the results of *ab initio* calculations show excellent agreement when compared with data obtained by rigorous structural analysis of X-ray and other diffraction results. We find that the available CALPHAD model parameters representing alloy energetics vary significantly from one assessment to another in these systems. These discrepancies underscore the point that CALPHAD modeling generally requires accurate thermodynamic data over the entire composition range to derive unique parameter sets; in the absence of such complete databases the parameters will depend on judgments made by the assessor in optimizing the thermodynamic model parameters. In such cases, the present results demonstrate how first-principles calculations can be employed as a viable framework for greatly augmenting available thermodynamic data for intermetallic phases in the construction of accurate thermodynamic databases.

1.A.2. Zero-temperature Phase Stability of Al-Zn-TM Intermetallics with $L1_2$, DO_{22} and DO_{23} Structures

Two approaches to the first-principles modeling of phase stability of three ($L1_2$, DO_{22} and DO_{23}) competing structures were employed. In the first approach, periodic supercell models were employed where several crystallographically equivalent sites are created by repeating the original unit cell along the principle lattice directions and the energy of compounds with site-substituted species are derived at discrete compositions. In the second approach, *ab initio* total energy calculations are combined with statistical methods within the framework of the cluster expansion formalism.

The results of supercell and cluster expansion calculations are summarized in Fig. 2 by plotting the calculated heats of formation of $L1_2$, DO_{22} and DO_{23} phases along the pseudo-binary sections (a) Al_3Ti-Zn_3Ti, (b) Al_3Zr-Zn3Zr, (c) Al_3Hf-Zn_3Hf [14]. Figure 2(a) shows good overall agreement between the

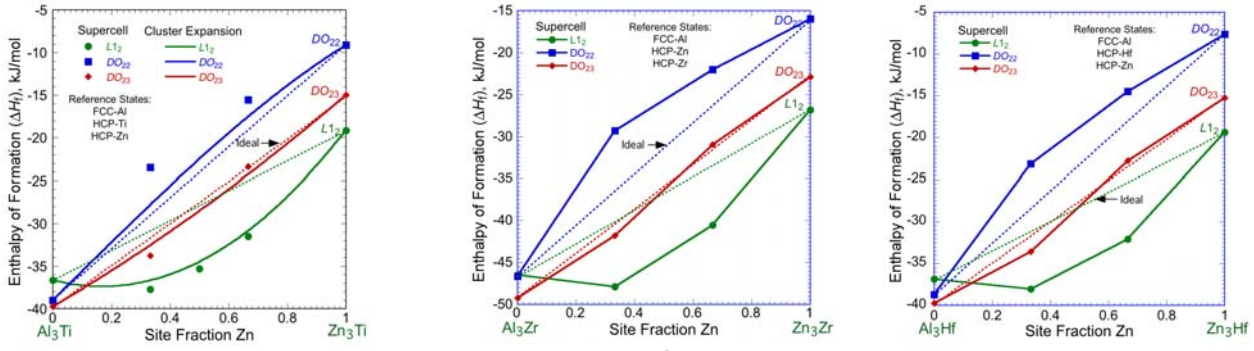

Figure 2. *Ab initio* calculation of heat of formation of $L1_2$, DO_{22} and DO_{23} phases along the pseudo-binary sections (a) Al_3Ti-Zn_3Ti, (b) Al_3Zr-Zn_3Zr, (c) Al_3Hf-Zn_3Hf. Figure 2(a) gives a comparison between the results of supercell calculations and those predicted by the cluster expansion for random mixing, showing good overall agreement [14].

supercell results and those predicted by the cluster expansion for random mixing of Al and Zn atoms. The supercell calculations show that the trend in the relative stability of $L1_2$, DO_{22} and DO_{23} phases is similar in all cases considered. As Al (or Zn) is replaced by Zn (or Al), the thermodynamic stability of $L1_2$ is enhanced while the opposite is true for DO_{22} and DO_{23} structures.

To understand the electronic origin of the enhanced stability of $L1_2$ and the reduced stability of the tetragonal DO_{22} and DO_{23} structures arising from the addition of Zn in Al_3TM, we have calculated the electronic densities of states (DOS) [14]. As an example, the total DOS of Al_3Ti and $(Al_{0.667}Zn_{0.333})_3Ti$, are shown in Fig. 3. In $L1_2$-Al_3Ti, the Fermi level is on the right (higher energy) of the pseudo-gap associated with the hybridization between Al *s-p* and TM *d* electrons, and thus lies within the antibonding states. In DO_{22}-Al_3Ti, the Fermi level is on the left (lower energies) of the pseudo-gap, within the bonding states, while in DO_{23}-Al_3Ti the Fermi level is very close to the minimum of the pseudo-gap. As shown in Figure 3(b), when one-third of the Al-sites are substituted by Zn, which has the effect of reducing the average number of valence electrons per atom in the systems, the Fermi level in $L1_2$ structure shifts out of the antibonding states into the pseudo-gap; in DO_{22} and DO_{23} structures the Fermi level is shifted the left of pseudo-gap depleting the degree of occupation of the bonding states. These results are consistent with the idea that the most stable phase is the one which optimizes the filling of bonding states within a rigid band model.

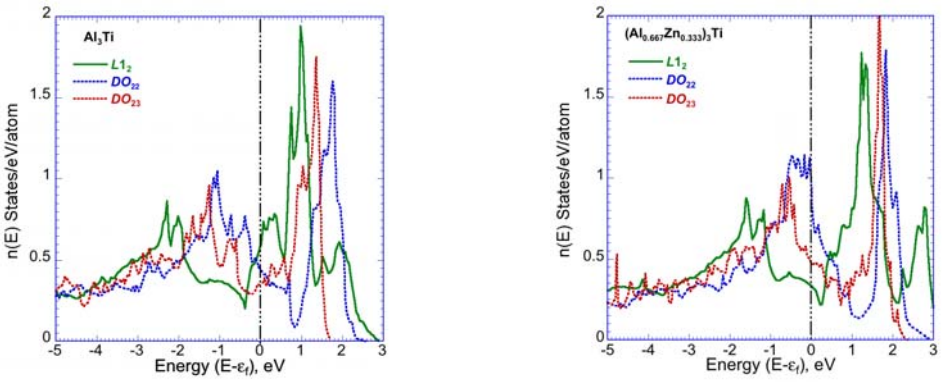

a b

Figure 3. Total density of states for (a) Al_3Ti and (b) $(Al_{0.667}Zn_{0.333})_3Ti$ [14].

1.A.3. Finite-temperature Phase Stability of Al-TM Systems

In a*b-initio* phase diagram calculations at finite temperatures, vibrational entropy S_{vib} contributions to the free energy often play an important role [9,10]. This is particularly essential in predicting the solubility limits in (Al), with respect to both metastable and stable Al-TM phases. In this study, the vibrational entropy S_{vib} of $L1_2$, DO_{22} and DO_{23} structures and other representative ordered configurations are calculated by the *ab-initio supercell* ("frozen phonon") technique within harmonic phonon theory. The results are summarized in Fig. 4. The large and negative formation vibrational entropies $\Delta S_{vib} = S_{vib}(Al_xTM_{(1-x)}) - xS_{vib}(Al) - (1-x)S_{vib}(TM)$ for all of the ordered structures are consistent with the strong ordering tendencies displayed by these Al-TM (TM=Ti, Zr and Hf) systems. Specifically, the formation of strong Al-TM bonds in the compounds leads to a lower vibrational entropy relative to the constituent pure elements.

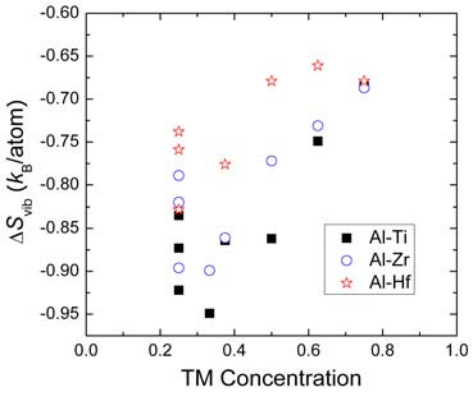

Figure 4. Formation vibrational entropy of twenty three selected ordered structures in Al-TM (TM=Ti, Zr and Hf) alloys [12].

To model vibrational entropies in the disordered solid solutions the cluster expansion (CE) technique was employed. Normally tens of reliable ordered structure vibrational entropies are required to derive well-converged cluster expansions. A transferable force constant (TFC) approach [17] is, thus, developed to efficiently compute these vibrational entropies [18]. For the 23 ordered structures calculated by *ab-initio* supercell methods (Fig. 4), it is observed the first nearest neighbor atomic bond force constants are strongly correlated with the bond length and TM concentration. Figure 5 shows this correlation for the Al-Zr system. By making use of this correlation we can circumvent the most time-consuming part of the force-constant calculation in the *ab-initio supercell* method by estimating the bond force constants from

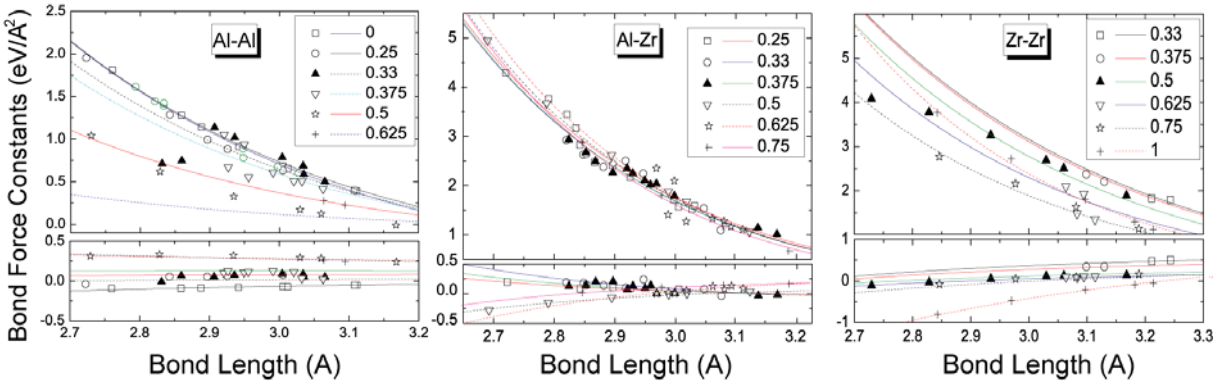

Figure 5. Calculated nearest-neighbor force constants vs. bond length and Zr concentration. Results with positive values correspond to bond stretching stiffness, while the negative values are bending stiffness. The inset labels represent different Zr concentrations in Al [18].

the equilibrium bond length and the TM concentration in Al. The error associated with such a TFC approach is found to be reasonably small, about $0.1k_B$/atom (<15% compared with ΔS_{vib} in Fig. 4).

A total of 40-50 vibrational entropies were calculated for a variety of ordered structures by the TFC method and used in fitting the interactions parameters in a cluster expansion of S_{vib}. With this approach, well-converged cluster expansions were derived with prediction errors limited to about ±0.07-0.09k_B/atom. Table 1 lists the results of formation entropy ΔS_{vib} and formation enthalpy ΔH values for stable and metastable precipitate phases and dilute solutions.

Table 1. Formation enthalpies ΔH and formation vibrational entropies ΔS_{vib} for the precipitates and dilute solutions in Al-TM (TM=Ti, Zr and Hf) systems

	ΔH (eV/TM atom)				ΔS_{vib} (k_B/TM atom)			
	$L1_2$	$D0_{22}$	$D0_{23}$	Dilute Solution	$L1_2$	$D0_{22}$	$D0_{23}$	Dilute Solution
Al-Ti	-1.641	-1.718	-1.734	-1.13	-3.365	-3.568	-3.731	-2.518
Al-Zr	-1.964	-1.968	-2.076	-1.25	-3.354	-3.356	-3.697	-1.000
Al-Hf	-1.609	-1.685	-1.727	-0.954	-2.989	-3.211	-3.402	-0.837

Phase boundaries involving the dilute solution (Al) and $L1_2$, DO_{22} and DO_{23} Al_3TM phases are calculated with the model presented in Ref. 19 (for Al-Sc system) and the data in Table 1. Figure 6 plots the results. For all three systems, the vibrational entropy stabilizes the dilute solution phases, and consequently decreases the transition temperature and increases the solubility limits remarkably. In the Al-Ti system, DO_{22} is the stable phase above 900K. Our phase boundary (red solid line) agrees well with the equilibrium experimental results. Similar agreement is found in Al-Zr and Al-Hf system for the stable DO_{23} phase boundaries. The very dilute solubility of Zr (compared with Al-Ti alloy) leads to large scatter in the experimental measurements. In light of the agreement demonstrated between experiment and theory for Al-Ti and Al-Zr systems, as well as the significant scatter observed between the experimental measurements for Al-Zr, we expect that the deviation apparent between theory and experiment for Al-Hf may be indicative of experimental difficulties associated with achieving equilibrium (note the agreement improves at higher temperatures where diffusion is more rapid). The accurate descriptions of the stable phase boundaries suggest the reliability of our predictions for the metastable $L1_2$ phase boundaries. The two component meta-stable $L1_2$ phase boundaries can thus be integrated in multi-component thermodynamic databases for design of ternary $L1_2$-strengthened alloys.

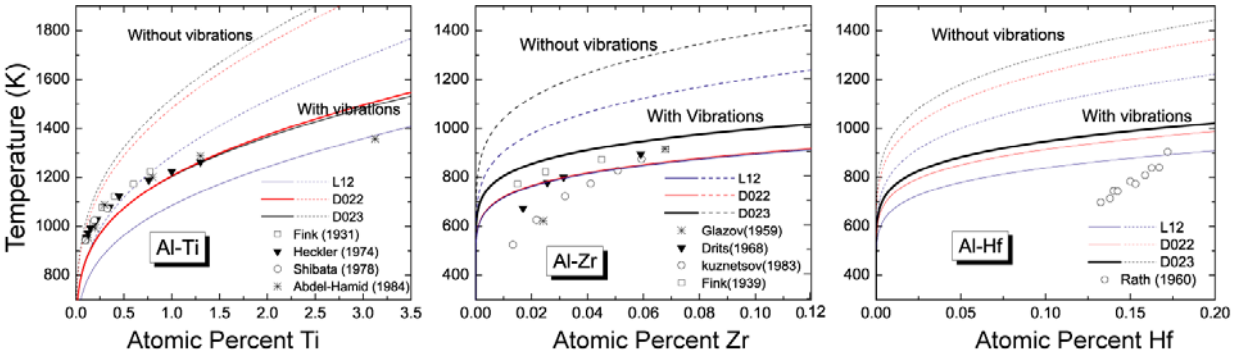

Figure 6. The solvus boundary of (Al) in Al-TM systems calculated by first-principles methods. The solvus boundary with and without vibration effect are compared for $L1_2$, DO_{22} and DO_{23} phases. The symbols represent the experimental measurements [18].

1.B. Experimental Verification of *Ab Initio* Phase Stability

To test the validity of our *ab initio* phase-stability calculations, we have carried out selected experiments using an alloy of Al-5 mass% Zn-0.2 mass% Zr. The alloy was prepared by arc melting using master alloys of Al-Zn and Al-Zr. The as-cast alloy was aged at 400˚C for 500 hrs. Thin foils of the aged alloy were examined in a conventional TEM (Hitachi 8100) and in an analytical electron microscope (Hitachi HF-2000) equipped with an EDS detector.

Figure 7(a) shows a selected area diffraction pattern along the [001] zone axis in which (100)-type superlattice reflections confirm the presence of $L1_2$-type precipitates. Figure 7(b) is the dark-field TEM

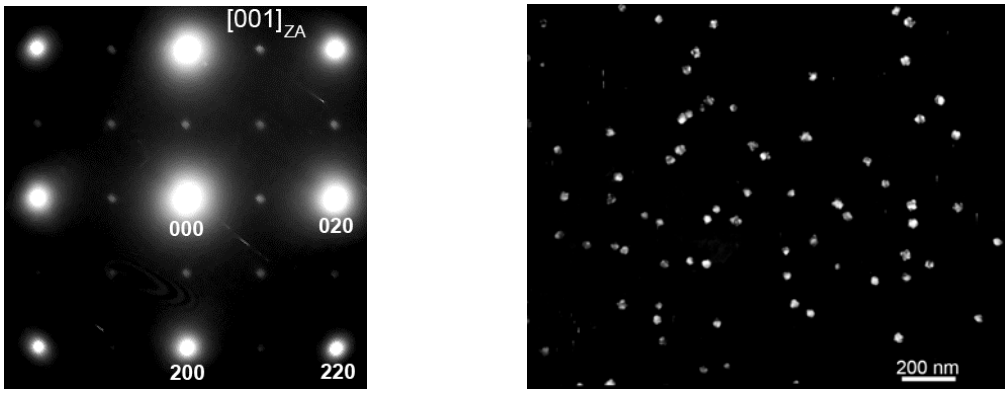

a b

Figure 7. Transmission electron microscopy of Al-5 mass% Zn-0.2 mass% Zr alloy, as-cast followed by aging at 400˚C for 500 hrs: (a) diffraction pattern showing the presence of $L1_2$ superlattice spots, and (b) dark-field micrograph using (100)-type reflection showing nanoscale coherent $L1_2$ precipitates.

micrograph, taken using (100)-type superlattice reflection, showing nano-scale and fully coherent $L1_2$ precipitates. Typically, the precipitate diameter lies in the range of 20 to 30 nm. However, many precipitates show dendritic morphology, instead of being cuboidal, with preferential growth along <110>-type directions, a characteristic feature of precipitates growing at a low supersaturation. This type of morphology has also been observed in $L1_2$-Al_3Sc precipitates [19].

While the formation of metastable $L1_2$ precipitates in binary Al-Zr, Al-Zr-Ti, Al-Zr-V alloys is well established in literature [20,21], a more fundamental and important result is revealed in the EDS analysis of matrix and precipitate in a dedicated analytical electron microscope with nano-probe capability. Figure 8(a) and 8(b) shows the EDS spectra from (Al)-matrix and $L1_2$ precipitate, respectively. A qualitative comparison of the relative heights of Zn-K or Zn-L peak clearly shows that the Zn-partitioning ratio (precipitate/matrix) lies between 4 and 5. This is very significant, because our *ab initio* modeling predicts that the critical amount of Zn needed for maximum stability of the $L1_2$ precipitate is about 12 at.%. These preliminary results clearly demonstrate that it is possible to obtain "thermodynamically stable" $L1_2$ precipitates in Al-Zn-Zr alloys, which is predicted by the electronic structure calculations of competing fcc-based ordered structures. These precipitates were predicted (designed) by computation from first principles and then verified experimentally.

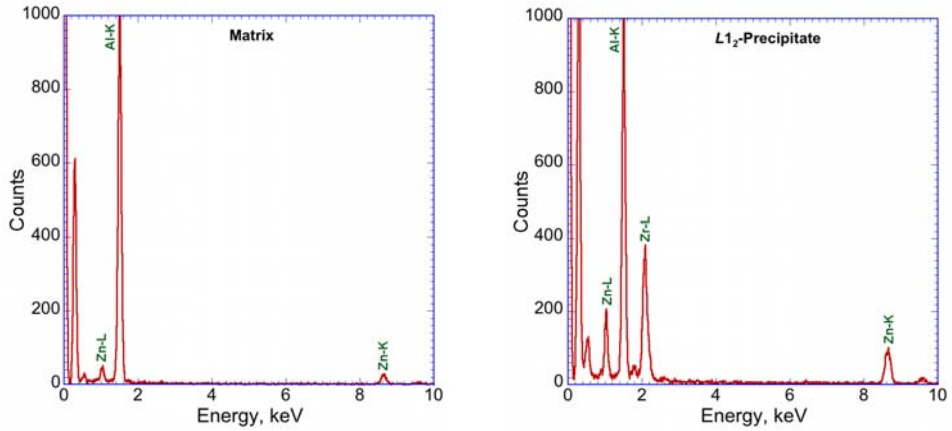

a b

Figure 8. EDS spectra in an analytical electron microscope: (a) from (Al) matrix, and (b) from $L1_2$ precipitate. The EDS spectra were collected using a probe size of about 5 nm. Only the precipitates protruding out of the edge of thin-foil were analyzed so as to eliminate the effect of matrix.

2. Conclusions

We have carried out the most comprehensive study of phase-stability in Al-TM (TM=Ti.Zr,Hf) systems, both at zero-temperature and at finite temperatures, using *ab initio* techniques. This led to, for the first time, the calculation of stable and metastable (Al) solvus boundaries.

State-of-the-art *ab initio* phase-stability calculations are also performed for the Al-Cu-TM and Al-Zn-TM (TM=Ti.Zr,Hf) systems. To investigate the phase stability involving $L1_2$, DO_{22} and DO_{23} structures in ternary systems, we have used both supercell approach and sublattice cluster expansion technique. Both results agree well with each other. Zero-temperature ab initio total energy calculations demonstrate that Zn stabilizes $L1_2$ structure in Al_3TM. The electronic origin of this structural stabilization is demonstrated by calculating the density of states (DOS).

Limited experimental data, in prototype Al-Zn-Zr alloys, confirm that indeed due to a significant partitioning of Zn in Al_3Zr, the $L1_2$ phase can be stabilized. However, further modeling and experimental studies are needed to understand the phase stability, microstructure dynamics, optimum alloy composition and processing in Al-Zn-TM (TM=Ti.Zr,Hf) systems. Remaining to be done are optimizing the volume fraction and composition of this precipitate to give best creep resistance and then to add it to the Al-Ni alloy described in the Introduction.

PART 2. Ab Initio Calculations and Experiments in Respect to Stability and Elastic Properties of $L1_2$-$(Al,Cu)_3(Ti,Zr)$ Phases – G. Ghosh and S. Vaynman

Summary

The total energies and equilibrium cohesive properties of $L1_2$, DO_{22} and DO_{23} structures along Al_3Ti-Al_3Zr and Al_3X-Cu_3X (X=Ti, Zr) sections are calculated from first-principles employing electronic density-functional theory (DFT), ultrasoft pseudopotentials and the generalized gradient approximation. Calculated heats of formation are consistent with a narrow field of stability of the $L1_2$ structure at 12.5 at % Cu for ternary $(Al,Cu)_{0.75}Zr_{0.25}$ and $(Al,Cu)_{0.75}Ti_{0.25}$ intermetallics at low temperatures. Experimentally, samples homogenized at 1000°C establish a more extensive stability field for the $L1_2$ phase in quaternary alloys with Cu concentrations ranging from 6.7 to 12.6 at % Cu. Two $L1_2$ phases were observed in as cast alloys with near equal amounts of Ti and Zr, as well as alloys homogenized at 1000°C. Good agreement is obtained between calculated and measured values of lattice parameters and elastic moduli. These results demonstrate high accuracy of *ab initio* calculations for phase stability, lattice parameters and elastic constants in multicomponent trialuminide intermetallics.

2.1. Introduction

Cubic $L1_2$-structured trialuminides have long been of interest because of their possible use as low-density, high-temperature structural materials. The inherent brittleness of trialuminides, however, has severely limited their use in such applications. Many of the efforts to increase the ductility of these alloys have focused on identifying alloying additions that can lead to the stability of the cubic $L1_2$ phase, rather than the tetragonal (DO_{22} and DO_{23}) structures that form in most binary trialuminides. Since there are more independent slip systems in the $L1_2$ structure than in tetragonal structures, $L1_2$ intermetallics have been sought due to the possibility that they can be more ductile than their tetragonal counterparts.

Under equilibrium conditions, both Al_3Ti and Al_3Zr form tetragonal crystal structures, namely DO_{22} and DO_{23}, respectively. It is well known that addition of fourth-period transition elements including Cu to these intermetallics leads to the stability of the high-symmetry cubic $L1_2$ phase [2, 12, 22-35]. These findings raise the intriguing possibility that such additions to Al-Ti-Zr alloys could give rise to the formation of a stable $L1_2$ precipitate microstructure. Earlier studies have shown that the coarsening rate of $L1_2$ precipitates in Al-Ti-Zr alloys [21] is much lower than in Al-Zr alloys [20]; this effect could be attributed to the lower diffusivity of Ti in Al, relative to Zr, as well as the lower misfit inherent in Al-Zr alloys with Ti additions. It is known that quaternary $L1_2$ intermetallic compounds that contain both Ti

and Zr atoms along with fourth-period transition elements can be synthesized with a lattice parameter that matches that of aluminum. Since coarsening rate and interfacial energy are influenced by the misfit strain, it is desirable to design precipitation-strengthened alloys with near-zero misfit strain.

These experimental results motivated Hong and Freeman [36] to investigate the effect of Cu additions to Al_3Ti on the phase stability and bonding mechanisms in the $L1_2$ and DO_{22} structures by means of *ab initio* electronic-structure calculations. As a part of our research on the computationally-assisted design of new Al-base alloys, we present the results of *ab initio* phase stability and elastic properties of $Al_3(Ti,Zr)$, $(Al,Cu)_3Ti$ and $(Al,Cu)_3Zr$ alloys. Specifically, we consider the relative stability of the three competing fcc-based ordered structures $L1_2$, DO_{22} and DO_{23}. In parallel with the computational work, we have undertaken experimental research focusing on ternary and quaternary intermetallics containing Al, Ti, Zr and Cu. The computed and measured lattice parameters and isotropic elastic moduli of the ternary alloys are compared and related to the compositions of these intermetallics. The quaternary alloys were investigated because they are candidate reduced-misfit-strain precipitates in cast Al-base alloys.

2. Computational methodology

2.1. *Ab initio* total energy calculations

The *ab initio* calculations presented here are based on electronic density-functional theory (DFT), and have been carried out using the *ab initio* total-energy and molecular-dynamics program VASP (Vienna *ab initio* simulation package) developed at the Institut für Materialphysik of the Universität Wien [7,8]. The current calculations make use of the VASP implementation of ultrasoft pseudopotentials [10], and an expansion of the electronic wave functions in plane waves with a kinetic-energy cutoff of 281 eV. For the transition metals the pseudopotentials employed in this work treated the following states as valence: Ti-4*s*, 4*p* and 3*d* and Zr-5*s*, 5*p* and 4*d*. In a few cases calculations were conducted using alternative Ti and Zr pseudopotentials including 3p and 4p semi-core states, respectively. All calculated results were derived employing the generalized gradient approximation (GGA) for exchange and correlation due to Perdew and Wang [37`]. Brillouin-Zone integrations were performed using Monkhorst-Pack [38] *k*-point meshes, and the Methfessel-Paxton [39] technique with a 0.1 eV smearing of the electron levels. For each structure, tests were carried out using different *k*-point meshes to ensure absolute convergence of the total energy to within a precision of better than 2.5 meV/atom (0.25 kJ/mole). As an example, the *k*-meshes for Al_3Ti having $L1_2$, DO_{22} and DO_{23} structures were 20x20x20, 22x22x10 and 21x21x5, respectively. Depending on the structure, up to 390 *k*-points were used in the irreducible Brillouin zone. Total energies of each structure were optimized with respect to the volume, unit cell-external degree(s) of freedom (i.e., the unit-cell shape) and unit cell-internal degree(s) of freedom (i.e., Wyckoff positions) as permitted by the space-group symmetry of the crystal structure. Such structural optimizations were iterated until the atomic forces were less than 4 meV/Å in magnitude, ensuring a convergence of the energy with respect to the structural degrees of freedom to better than 2.5 meV/atom (0.25 kJ/mole). With the chosen plane-wave cutoff and *k*-point sampling the reported formation energies are estimated to converge to a precision of better than 5 meV/atom (0.5 kJ/mole). The approach outlined in this section was used to compute formation energies, lattice parameters and elastic moduli at zero temperature.

2.2. Equation of state and formation energy

We take the zero-temperature formation energy (ΔE^{ϕ}) of an intermetallic as a key measure of the relative stability of competing structures (ϕ_1, ϕ_2, ϕ_3). This quantity is evaluated relative to the composition-averaged energies of the pure elements in their equilibrium crystal structures. For example, the formation energy of a ternary intermetallic, $Al_pCu_qTM_r$ where *p*, *q* and *r* are integers, is given by:

$$\Delta E^{\phi}(Al_pCu_qTM_r) = \frac{1}{p+q+r} E^{\phi}_{Al_pCu_qTM_r} - [\frac{p}{p+q+r} E^{\theta}_{Al} + \frac{q}{p+q+r} E^{\theta}_{Cu} + \frac{r}{p+q+r} E^{\psi}_{TM}] \qquad (1)$$

where $E^{\phi}_{Al_pCu_qTM_r}$ is the total energy (per formula unit) of $Al_pCu_qTM_r$ with structure ϕ ($L1_2$ or DO_{22} or

DO_{23}), E^{θ}_{Al} is the total energy per atom of Al with the fcc (θ) structure, E^{θ}_{Cu} is the total energy per atom of Cu with the fcc (θ) structure and E^{ψ}_{TM} is the total energy per atom of TM (=Ti, Zr) with the hcp (ψ) structure.

The zero-temperature equation of state (EOS) defines the pressure-volume relationship. We have used the EOS due to Vinet *et al* [36] who assumed the interatomic interaction-versus-distance relation in solids can be expressed in terms of a relatively few material constants. In the EOS of Vinet *et al* [40] the pressure P is expressed in terms of isothermal bulk modulus (B_o), its pressure derivative (B'_o) and a scaled quantity (x):

$$P = 3B_o x^{-2}(1-x)\exp[\eta(1-x)] \tag{2}$$

with $x = (V/V_o)^{1/3}$ and $\eta = 3/2(B'_o - 1)$, where V_o is the equilibrium volume. Based on Eq. (2) and the relations between pressure and energy, the total energy (E) and volume-dependence of the bulk modulus can be expressed as

$$\mathrm{E(V) - E(V_o)} = \frac{9\mathrm{B_o V_o}}{\eta^2}\{1-[\eta(1-\mathrm{x})]\exp[\eta(1-\mathrm{x})]\} \tag{3}$$

2.3. Calculation of single-crystal elastic constants

Generally, the single-crystal elastic constants can be obtained by *ab initio* electronic-structure methods by calculating the total energy as a function of appropriate lattice deformations. Depending on the crystal system and the type of imposed lattice deformation, the curvature of the total energy versus strain curves defines either a particular elastic constant or a combination of elastic constants.

The internal energy ($E(V,\{e_i\})$) of a crystal under an infinitesimal strain e_i, referenced to the energy of the equilibrium geometry, can be written as

$$E(V,\{e_i\}) = E(V_o,0) + \frac{V_o}{2}\sum_{ij} C_{ij}e_i e_j + ... \tag{4}$$

where V_o is the volume of the unstrained system with $E(V_o,0)$ being the corresponding energy, C_{ij}s are the single crystal elastic constants, and the members of strain tensor $\boldsymbol{\varepsilon}\{e_i,e_j,..\}$ are given in Voigt notation.

For the $L1_2$ phase with cubic lattice symmetry, there are three single crystal elastic constants, C_{11}, C_{12} and C_{44}. For the DO_{22} and DO_{23} phases with tetragonal lattice symmetry, there are six single crystal elastic constants, C_{11}, C_{12}, C_{13}, C_{33}, C_{44} and C_{66}. Mehl *et al* [41] summarized the appropriate lattice deformations needed to derive the C_{ij}s in these two crystal systems. For each structure, we have calculated total energies by imposing appropriate strains up to ±3% at 0.5% interval. The total energies versus strain were fit with the functional forms provided by Mehl *et al* to extract the elastic moduli.

2.4. Relationship between single crystal and polycrystalline elastic constants

For an elastically anisotropic cubic phase, which is the case for all $L1_2$ phases in this study, several relations between single crystal elastic constants, C_{ij}, and the isotropic shear modulus (μ) have been proposed. The most notable ones are due to Voigt [42] who assumed uniform local strain, and due to Reuss [43] who assumed uniform local stress. Despite wide usage, neither Voigt's nor Reuss's relation is believed to be exact. Hill [44] showed that Voigt's equation provides an upper limit of μ while Reuss's equation gives a lower limit of μ. Accordingly, Hill suggested an averaging by either the arithmetic or the geometric mean of these two limits.

To mimic an ideal isotropic behavior (completely random orientation distribution), Hershey [45] modeled the elasticity of a polycrystalline aggregate in terms of the elasticity of individual grains with

spherical boundaries, and proposed the following quartic equation

$$64\mu_H^4 + 16(4C_{11} + 5C_{12})\mu_H^3 + [3(C_{11} + 2C_{12})(5C_{11} + 4C_{12}) - 8(7C_{11} - 4C_{12})C_{44}]\mu_H^2$$
$$-(29C_{11} - 20C_{12})(C_{11} + 2C_{12})C_{44}\mu_H - 3(C_{11} + 2C_{12})^2(C_{11} - C_{12})C_{44} = 0 \quad (5)$$

Hershey's method, proposed independently by Kröner [46], is viewed generally as exact. Accordingly, we have used this method to convert the single crystal elastic constants into isotropic shear moduli of the $L1_2$ phases.

Knowing bulk modulus (Eq. 3) and isotropic shear modulus (Eq. 5) values from *ab initio* data, we can calculate the Young's modulus (Y) and Poissons ratio (ϑ) of a polycrystalline aggregate of the $L1_2$ phases using the following relationships

$$Y = \frac{9B_o\mu_H}{3B_o + \mu_H} \quad (6)$$

$$\vartheta = \frac{1}{2}\frac{3B_o - 2\mu_H}{3B_o + \mu_H} \quad (7)$$

Like the cubic case, Voigt and Reuss limits of μ of a polycrystalline aggregate of tetragonal phases (DO_{22} and DO_{23}) can also be calculated from the C_{ij} data (for example, see reference 37), which in turn can be used to calculate the corresponding Y and ϑ as given by Eqs.6 and 7.

2.5. *Ab initio* phase stability

The results of *ab initio* calculations for binary intermetallics are summarized in Table 2. In the case of Al_3Ti, we find that the DO_{23} phase has the lowest energy. This result is consistent with the findings of Amador *et al* [47] and Colinet and Pasturel [48] who emphasized the important role of relaxation energies (i.e., the energy reduction associated with optimization of the lattice parameters and cell-internal positions) in governing the relative stability of these competing structures. While there is consensus amongst the different calculations, the theoretical results are in apparent discrepancy with experimental observations which have established $D0_{23}$-Al_3Ti to be a transient (metastable) phase [49-51] at intermediate temperatures, which transforms to the equilibrium $D0_{22}$ structure. A possible reason for this apparent discrepancy between experiment and theory could be that entropy differences between the competing phases in Al_3Ti are large enough to reverse their relative stability at the temperatures where experiments have been conducted. Indeed, the role of vibrational entropy in reconciling a similar apparent discrepancy between theory and experiment for the competing phases of Al_2Cu was demonstrated by Wolverton and Ozolins [16]. In the case of Al_3Zr, we find that the DO_{23} phase has the lowest energy. This result is consistent with the findings of the theoretical work of Alatalo *et al* [52] and Colinet and Pasturel [53], as well as experimental observations. In the case of Cu_3Ti and Cu_3Zr, the DO_{22} phase has the lowest calculated energy. While the formation energies of DO_{23} phases are weakly negative in these systems, they are positive for the $L1_2$ phase, which is therefore thermodynamically unstable with respect to the constituent elements.

Table 2. Calculated zero-temperature cohesive properties of Al_3Ti, Al_3Zr, Cu_3Ti and Cu_3Zr with DO_{23}, DO_{22} and $L1_2$ structures. The EOS parameters, V_o (x10^{-3} nm^3/atom), B_o (x10^{10} N/m^2) and B_o', are defined by Eq.(3). The reference states for the formation energy (ΔE) are fcc-Al, fcc-Cu and hcp-(Ti, Zr)

Phase	Strukturbericht Designation		EOS Parameters V_o	B_o	B_o'	ΔE (kJ/mol)	Lattice Parameters a	c
Al_3Ti	DO_{23}	15.819	10.31	4.08		-39.656	0.38962	1.66713
	DO_{22}	15.929	10.30	4.15		-38.895	0.38399	0.86399
	$L1_2$	15.737	10.36	4.12		-36.583	0.39779	
	$L1_2$§	15.790	10.34	3.96		-36.329	0.39824	
Al_3Zr	DO_{23}	17.366	10.25	3.98		-49.106	0.40082	1.72969
	DO_{22}	17.581	10.18	4.05		-46.552	0.39479	0.90214
	$L1_2$	17.190	10.31	3.93		-46.418	0.40968	
	$L1_2$¶	17.355	10.03	4.02		-44.760	0.41099	
Cu_3Ti	DO_{23}	13.270	13.47	4.88		-1.503	0.41590	1.19665
	DO_{22}	13.132	13.92	4.66		-7.390	0.42072	0.59347
	$L1_2$	13.558	12.88	4.96		10.387	0.37852	
Cu_3Zr	DO_{23}	14.818	12.36	4.70		-3.216	0.43687	1.24646
	DO_{22}	14.594	13.09	4.20		-11.598	0.43566	0.61588
	$L1_2$	15.220	11.82	3.92		9.994	0.39339	
	$L1_2$¶	15.446	11.71	4.49		10.980	0.39533	

§: obtained with Ti pseudopotentials including 3p semicore states
¶: obtained with Zr pseudopotentials including 4p semicore states

As a part of this research, we are interested in the effect of Cu on the relative stability of Al_3Ti and Al_3Zr in the $L1_2$, DO_{22} and DO_{23} structures. In addition, we are also interested in the phase stability of Al_3(Ti, Zr) compounds in these three competing structures. To examine the relative stability of intermetallic phases at off-stoichiometric compositions, two approaches to modeling the inherent compositional disorder by *ab initio* methods include: (i) total energy calculations combined with statistical methods, such as the cluster expansion method [54], to predict thermodynamic and cohesive properties as a function of composition and temperature, and (ii) supercell methods where several crystallographically equivalent sites are created by repeating the unit cell along the principal lattice directions and total energy calculations are conducted with a subset of the equivalent sites occupied by the additional solute/solvent atoms required to give the desired composition. While the first technique allows prediction of various properties as a function of composition and temperature in a continuous manner, the second technique allows prediction of properties only at discrete compositions and zero temperature. Nonetheless, the second approach is computationally less demanding for multicomponent systems and has thus been applied in the current work.

In this study, we have calculated the total energies of ternary alloys using supercells of 2x2x2 for $L1_2$, and 2x2x1 for DO_{22} and DO_{23} phases. Following the findings of Hong and Freeman [32] who reported that the substitution of Ti by Cu increases (more positive) the total energy, we have calculated the total energy of selected ternary alloys formed by putting Cu atoms on the Al sublattice only. Thus, in the case of $L1_2$ supercell we have put Cu in one or more 3*c*-type sites, and in the DO_{22} supercell we have put Cu in the 2*b*-type sites only (the calculations of Hong and Freeman established that Cu substitution on the alternative Al 4*d*-type sites was less favorable than on the 2*b*-type sites). In the case of DO_{23} structure, it

was necessary to sample all unique sites in the Al sublattice in order to obtain the minimum energy configuration. In Al_3X or Cu_3X phases with the DO_{23} structure, there are three non-equivalent sites (or Wyckoff position) where Al or Cu atoms can reside, and they are designated as 4*c* (0,0,0.5), 4*d* (0,0.5,0.25) and 4*e* (0,0,*z*). We have calculated total energies by placing the third element, Cu in Al_3Ti and Al_3Zr or Al in Cu_3Ti and Cu_3Zr, in all three sites, and then the configuration that gave minimum energy was used for the analysis of the relative phase stability. In the case of $(Al_{0.75}Cu_{0.25})_3Ti$, we find that the calculated total energies have the following order: $E_{Cu\ in\ 4c} > E_{Cu\ in\ 4e} > E_{Cu\ in\ 4d}$. The decrease in energy when Cu resides in 4*e* and 4*d* sites relative to that in the 4c site is 1.3 and 6.96 kJ/mol, respectively. On the other hand, in the case of $(Cu_{0.75}Al_{0.25})_3Ti$, we find that the total energy is in the following order: $E_{Al\ in\ 4d} > E_{Al\ in\ 4c} > E_{Al\ in\ 4e}$. The decrease in energy when Al resides in 4*c* and 4*e* sites relative to that in the 4*d* site is 14.33 and 17.31 kJ/mol, respectively. A similar trend of site preference for Cu in $(Al_{0.75}Cu_{0.25})_3Zr$ and Al in $(Cu_{0.75}Al_{0.25})_3Zr$ was also found.

The results of *ab initio* phase stability calculations along the pseudo-binary sections Al_3Ti-Al_3Zr, Al_3Ti-Cu_3Ti, and Al_3Zr-Cu_3Zr are shown in Figures 9(a) to 9(c), respectively. As seen in Figure 9(a), the relative stability of DO_{23}, DO_{22} and $L1_2$ phases is rather monotonic across the Al_3Ti-Al_3Zr section, and there is only a slight positive deviation from ideal (linear) behavior. On the other hand, the relative stability of DO_{23}, DO_{22} and $L1_2$ phases along Al_3Ti-Cu_3Ti and Al_3Zr-Cu_3Zr show many interesting and non-monotonic features. The formation energies of DO_{23} and $L1_2$ phases show negative deviation from ideal behavior; implying that the addition of Cu increases the stability of these two phases; the effect is somewhat stronger in the $L1_2$ phases for Al-rich compositions. The effect of Cu addition on the formation energy of the DO_{22} phase is non-monotonic, it has a destabilizing effect on the Al-rich side while it enhances the stability of this phase on the Cu-rich side. Hong and Freeman [36] used linear muffin tin orbital (LMTO) method with local density approximation (LDA) to calculate the total energy and electronic structure of binary and ternary alloys. Their results on the formation energy of Al_5CuTi_2 with $L1_2$ and DO_{22} structures also show a similar trend as ours, but the magnitude of change in formation energy relative to Al_3Ti differs. They explained the effect of Cu on the relative stability of $L1_2$ and DO_{22} structures on the basis of the shift in the Fermi energy relative to the location of the bonding, nonbonding and antibonding states in Al_5CuTi_2 compared to their counterparts in Al_3Ti.

The zero-temperature energy calculations suggest that at least 12 at.% (16 site% in Al-sublattice) Cu in Al_3Ti and 15 at.% Cu (20 site% in Al-sublattice) in Al_3Zr is needed to stabilize $L1_2$ phase relative to the DO_{22} and DO_{23} phases. It is interesting to note that experimentally single-phase $L1_2$ microstructures have been observed in Al_5CuTi_2 [32,35] and $Al_{62}Cu_{13}Ti_{25}$ [23] alloys, where the Cu-contents are slightly above our calculated critical value of 12 at.%. While the correspondence between the calculations and experimental observations is encouraging, our predicted "critical" composition for the stability of the $L1_2$ phase should be considered as approximate, as we have performed total energy calculations at relatively few discrete compositions and at zero temperature, neglecting entropic and possible short-range-ordering effects. The calculation of the formation free-energies of these phases for ternary compositions using the cluster expansion technique would be expected to provide more accurate predictive values for the critical amount of Cu needed to stabilize the $L1_2$ phase in $(Al,Cu)_3Ti$ and $(Al,Cu)_3Zr$ alloys at given temperatures.

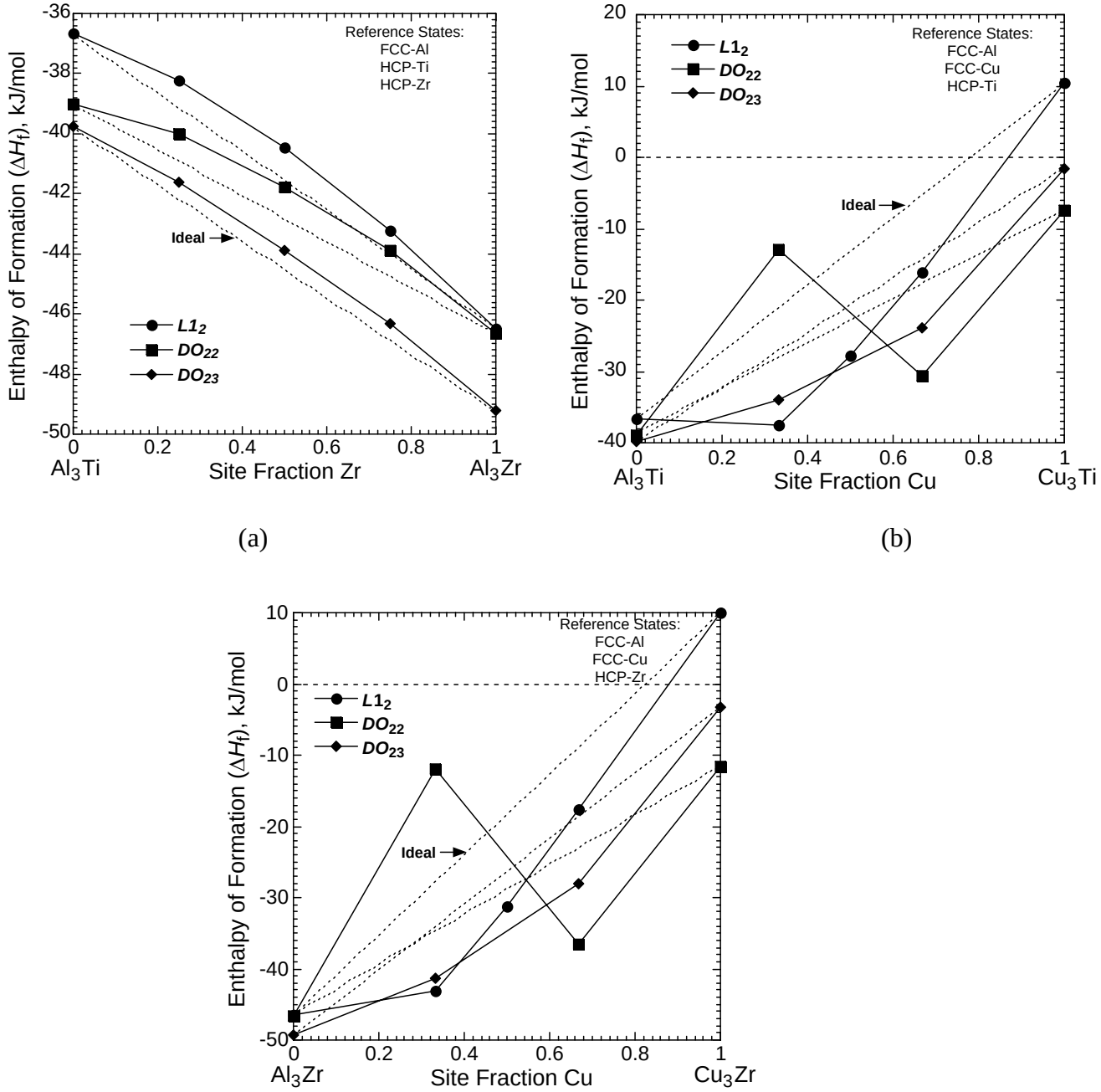

Figure 9. Ab-initio calculated zero-temperature formation energies for $L1_2$, DO_{22} and DO_{23} structures along (a) Al_3Ti-Al_3Zr, (b) Al_3Ti-Cu_3Ti, and (c) Al_3Zr-Cu_3Zr sections.

Figures 10(a) and 10(b) show the calculated $L1_2$ lattice parameter along Al_3Ti-Al_3Zr and Al_3X-Cu_3X (X=Ti,Zr) sections. Consistent with the trends shown in Figure 9 for the formation energies along three composition sections, the lattice parameters show a weakly positive deviation from linear composition dependence along Al_3Ti-Al_3Zr section, while a weakly negative deviation from linearity is obtained along Al_3X-Cu_3X (X=Ti,Zr) sections. The calculated lattice parameter value of 0.3935 nm for Al_5CuTi_2 agrees very well with the experimental value of 0.3927 nm [6,26]. Figure 10 provides valuable information related to the design of new Al-alloys containing fully coherent and coarsening resistant $L1_2$ precipitates, where it is desirable to design alloys with near-zero misfit strain. The calculations suggest that near equal concentrations of Zr and Ti in Al_3(Zr,Ti)-based $L1_2$ phases with a lattice parameter highly matched to the Al matrix.

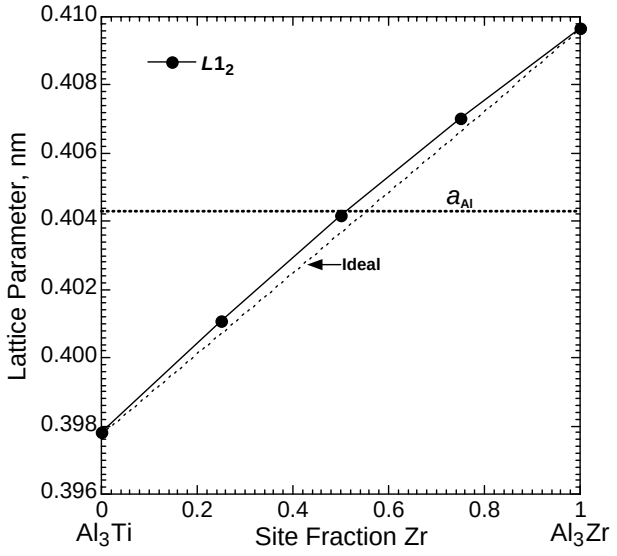

(a)

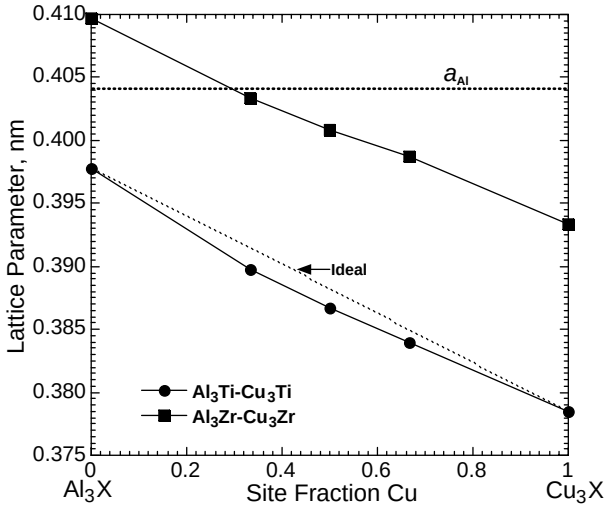

(b)

Figure 10. Calculated zero-temperature lattice parameter of the $L1_2$ structure along (a) Al_3Ti-Al_3Zr and (b) Al_3Ti-Cu_3Ti sections.

2.6. *Ab initio* elastic properties

The calculated single-crystal elastic constants (C_{ij}) are given in Table 3, along with the available experimental data and previously calculated values obtained by *ab initio* techniques. Fu [52,53] calculated the elastic constants of Al_3Ti ($L1_2$ and DO_{22}) using the full-potential linearized augmented plane-wave (FPLAPW) method within the LDA, while Clouet *et al* [54] calculated C_{ij} values for Al_3Zr ($L1_2$ and DO_{23}) using the full-potential LMTO within the LDA. In addition to these phases, we have also calculated elastic constants for $L1_2$-Cu_3Zr and Cu_3Ti; we find that the latter ($L1_2$-Cu_3Ti) is mechanically unstable, as C'=(C_{11}-C_{12})/2 is calculated to be negative.

Table 3. Single crystal elastic constants (x10^{10} N/m^2) of Al_3Ti (DO_{22} and $L1_2$), Al_3Zr (DO_{23} and $L1_2$), and Cu_3Zr ($L1_2$)

Phase	Strukturbericht Designation	Method	C_{11}	C_{12}	C_{13}	C_{33}	C_{44}	C_{66}	Reference
Al_3Ti	DO_{22}	FLAPW 20.20	8.80	6.00	24.30	10.0	14.50		[56,57]
	DO_{22}	US-PP 19.23	8.27	4.49	21.25	9.30	12.84		This study
	DO_{22}	Experiment	21.77	5.77	4.55	21.75	9.20	11.65	[58]
	$L1_2$	FLAPW 17.70	7.70	------	------	8.50	------		[57]
	$L1_2$	US-PP 18.39	6.26	------	------	7.35	------		This study
	$L1_2$	US-PP 18.52	6.25	------	------	7.32	------		This study§
Al_3Zr	DO_{23}	FP-LMTO 21.53	5.41	3.33	22.82	10.32	12.35		[57)
	DO_{23}	US-PP 21.44	5.76	3.36	20.17	8.22	9.83		This study
	DO_{23}	Experiment	20.88	7.05	4.91	20.83	8.72	10.22	[58]
	$L1_2$	FP-LMTO 18.73	5.57	------	------	9.51	------		[57]
	$L1_2$	US-PP 18.57	5.92	------	------	6.27	------		This study
	$L1_2$	US-PP 17.59	6.26	------	------	6.96	------		This study¶
Cu_3Zr	$L1_2$	US-PP 13.21	11.13	------	------	2.86	------		This study
	$L1_2$	US-PP 13.58	10.77	------	------	2.90	------		This study¶

§: obtained with Ti pseudopotentials including 3p semicore states
¶: obtained with Zr pesudopotentials including 4p semicore states

A comparison of experimental data for DO_{22}-Al_3Ti and DO_{23}-Al_3Zr [58] with our calculated values show a very good agreement for the values of C_{13}, C_{33}, C_{44} and C_{66} in Al_3Ti and C_{33}, C_{44} and C_{66} in Al_3Zr. In a previous calculation [52], these values were computed to be consistently higher than the present values, most likely due to the use of LDA approximation which leads to atomic volumes smaller than experiment and GGA calculations or these systems. On the other hand, in both the present (GGA) and previous (LDA) calculations for the values of C_{12} in Al_3Ti and Al_3Zr are predicted to be higher and lower, respectively, compared to the experimentally measured values.

The calculated polycrystalline elastic moduli of $L1_2$ phases are listed in Table 4. Fu [55] reported Y, m and ϑ for $L1_2$-Al_3Ti, but did not provide the exact methodology used to compute these moduli from the single-crystal elastic constants. Therefore, we have recalculated these quantities using his C_{ij} values, and the method described in section 2.4. Similarly, we have calculated the polycrystalline elastic moduli of $L1_2$-Al_3Zr using the C_{ij} values of Clouet *et al* [57]. From these quantities, the polycrystalline elastic moduli of the multicomponent $L1_2$ phase can be calculated with the assumption of linear superposition effect, which has been demonstrated to be a good approximation [59]. As an example, Figure 11 shows

the calculated bulk modulus along the Al_3X-Cu_3X section; a weakly positive deviation from ideal behavior is predicted.

Table 4. Calculated polycrystalline elastic moduli of $L1_2$ phases

Phase	B_o (x10^{10} N/m^2)	Y (x10^{10} N/m^2)	μ_H (x10^{10} N/m^2)	ϑ	Reference
Al_3Ti	11.80	17.50	7.10	0.200	[52]
	11.80	17.28	6.88	0.22	[52, this work]
	10.37	16.75	6.81	0.196	This study
	10.34	16.77	6.82	0.195	This study§
Al_3Zr	9.96	19.30	8.20	0.146	[54, this study]
	10.31	16.61	6.75	0.196	This study
	10.03	15.86	6.41	0.201	This study¶
Cu_3Zr	11.82	5.54	1.95	0.400	This study
	11.71	6.19	2.19	0.389	This study¶

§: obtained with Ti pseudopotentials including 3p semicore states
¶: obtained with Zr pseudopotentials including 4p semicore states

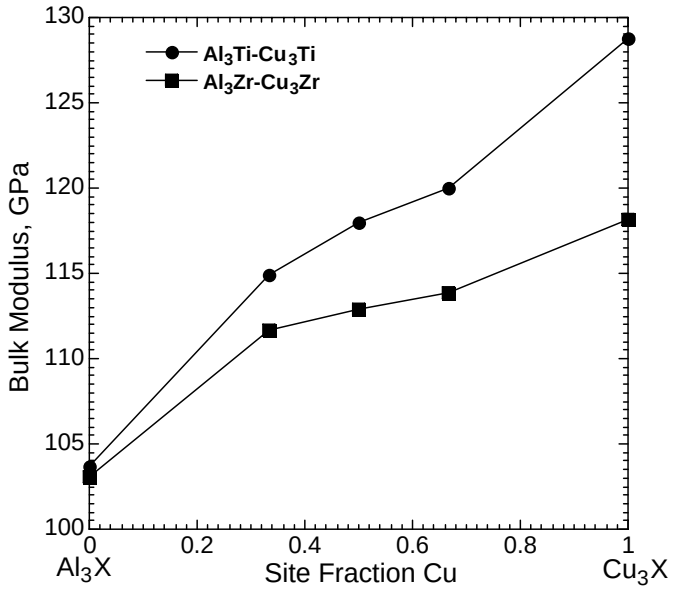

Figure 11. Calculated zero-temperature bulk modulus of the $L1_2$ structure along Al_3Ti-Cu_3Ti and Al_3Zr-Cu_3Zr sections.

2.7-1. Experimental procedure

The Al-Ti-Zr-Cu intermetallics were prepared from pure elements (99.9% at least) by arc-melting using a tungsten electrode in argon gas atmosphere and freezing in a water-cooled copper hearth to form 15 gram ingots. To insure homogeneity, the ingots were remelted 4-5 times. They were then homogenized

at 1000°C for 72 hours and quenched in water. The intermetallics were investigated in both as-cast and homogenized conditions.

The microstructures and compositions of the intermetallics were established by SEM/EDX (Hitachi S3500N Scanning Electron Microscope, Hitachi, Japan). The phases were identified and the lattice parameter determined by x-ray diffraction (XDS 2000, Scintag, Inc. USA).

The isotropic elastic moduli were measured by an ultrasonic pulse-echo technique that relates the measured sound wave velocities to the elastic moduli. We used an SR 9000 Ultrasonic Modulus Tester (Matec Instruments, Hopkinton, MA, USA) to measure the longitudinal and shear wave velocities. Axially-polarized and cylindrically-polarized transducers generated 50 MHz longitudinal and 20 MHz shear stress pulses, respectively. The reflections of the stress pulse from the front and back surfaces of the specimens were continuously monitored by a computer. The software system allowed the reflections to be frozen in the computer at any time from which the transit time (round trip) for reflections was measured and the velocity of longitudinal (ϑ_l) and shear waves (ϑ_s) were determined. Then, the isotropic shear modulus (μ), the Young's modulus (E), the bulk modulus (B), and the Poisson's ratio (ν) are given by:

$$\mu = \rho \vartheta_s^2 \tag{8}$$

$$E = 2(1+\nu)\mu \tag{9}$$

$$B = \frac{E\mu}{3(3\mu - E)} \tag{10}$$

$$\nu = \frac{2-R}{2(1-R)} \quad \text{with } R = \left(\frac{\vartheta_l}{\vartheta_s}\right)^2 \tag{11}$$

The density of the alloys was determined by measuring their weights in air (W_{air}) and in water (W_{water}) using the following equation:

$$\rho = \frac{W_{air}}{W_{air} - W_{water}} \tag{12}$$

2.7.2 Experimental results

Two sets of Al-Cu-Zr_x-$Ti_{(1-x)}$ alloys were prepared: one series contained approximately 8 at.% Cu and the other 12.5 at. % Cu. The content of Zr plus Ti was approximately 25 at.% in both series. The compositions of both sets measured by EDAX are given in Table 5. Two sets of alloy samples were made because as already noted previous experimental results and the *ab initio* computations in this study gave 12.5 at.% for the composition of Cu in the ternary $(Al\text{-}Cu)_{0.75}\ Ti_{0.25}$ phase with the $L1_2$ structure]. Similarly the present *ab initio* computations gave approximately 12.5 at. % Cu for thermodynamically stable $L1_2$ phase in the ternary $(Al\text{-}Cu)_{0.75}Zr_{0.25}$ system. In many other systems of $(Al\text{-}M)_{0.75}\ Ti_{0.25}$ where M is a 3d transition metal, an $L1_2$ phase is found at M of approximately 8 at.%.[26]

Tables 6 and 7 give the compositions of all of the phases and identify of $L1_2$ phases in the as-cast and homogenized (1000°C, 72 hrs.) conditions. Homogenization was done to approach equilibrium at that temperature. Some phases that resulted from solidification disappeared during homogenization as determined by SEM and X-ray diffraction. Pores were often observed associated with the disappearance of phases as others have seen in similar alloys [26]. The measured lattice parameters of the $L1_2$ phases are also given in the Tables 6 and 7. The as-cast samples will not be discussed since they do not represent equilibrium microstructures.

Comparing the 1000°C-homogenized samples in both alloys containing only Ti, $L1_2$ is the major phase present but the $L1_2$ phases contained 8.4 and 12.5 at.% Cu in alloys 8-1 and 12-1, respectively. The compositions of the cubic phases are slightly leaner in Al than present in the bulk alloy. The width of the $L1_2$ phase field is expected to increase on heating from low temperature. In alloys containing only Zr $L1_2$

phases containing 8 and 12.5% Cu were also found. In alloy 8-5 only the $L1_2$ was seen but alloy 12-5 contained small amounts of other phases.

Table 5. Chemical composition of alloys

Alloy	Chemical Composition (atomic %)			
	Al	Ti	Zr	Cu
8-1	69.2	23.0	0	7.2
8-2	67.7	19.5	5.2	7.6
8-3	67.9	12.3	11.9	7.9
8-4	68.2	6.3	17.8	7.7
8-5	67.3	0	24.7	8.0
12-1	61.3	26.3	0	12.4
12-2	61.2	18.2	7.9	12.7
12-3	61.5	12.9	12.7	12.9
12-4	61.8	8.6	17.3	12.3
12-5	61.8	0	25.4	12.8

Table 6. Chemical composition of phases observed in alloys 8-1 to 8-5 in as-cast and homogenized conditions

Alloy	Chemical Composition of Phases (atomic %)				Zr fraction, Zr/(Zr+Ti)	Crystal Structure	Lattice Parameter of $L1_2$ Phase, nm
	Al	Ti	Zr	Cu			
8-1 as-cast	70.1	23.0	0	6.9	0.00	$L1_2$	0.395
	76.9	22.5	0	0.6	0.00		
	55.7	3.5	0	40.8	0.00		
8-1 homogenized	66.0	25.6	0	8.4	0.00	$L1_2$	0.395
	72.4	26.4	0	1.2	0.00		
8-2 as-cast	67.0	21.0	4.3	7.7	0.17	$L1_2$	0.397
	67.2	19.2	7.3	6.1	0.28	$L1_2$	0.397
	74.0	20.2	4.8	1.0	0.19		
	69.0	3.0	0.4	27.6	0.12		
8-2 homogenized	67.7	19.5	5.2	7.6	0.21	$L1_2$	0.397
8-3 as-cast	68.2	9.5	15.2	6.7	0.62	$L1_2$	0.404
	66.9	14.5	9.6	9.0	0.40	$L1_2$	0.401
8-3 homogenized	68.2	8.7	14.8	8.3	0.63	$L1_2$	0.403
	67.9	15.1	9.8	7.2	0.39	$L1_2$	0.401
8-4 as-cast	69.0	4.0	19.7	7.3	0.83	$L1_2$	0.404
	67.8	8.0	16.7	7.5	0.68	$L1_2$	0.404
8-4 homogenized	68.2	4.8	19.3	7.7	0.80	$L1_2$	0.404
	68.2	6.6	17.6	7.6	0.73	$L1_2$	0.404
8-5 as-cast	67.9	0	24.7	7.5	1.00	$L1_2$	0.407
	74.6	0	24.3	1.1	1.00		
	61.6	0	32.5	5.9	1.00		
8-5 homogenized	67.3	0	24.7	8.0	1.00	$L1_2$	0.407

Table 7. Chemical composition of phases observed in alloys 12-1 to 12-5 in as-cast and homogenized conditions

Alloy	Chemical Composition of Phases (atomic %)				Zr fraction, Zr/(Zr+Ti)	Crystal Structure	Lattice Parameter of $L1_2$ Phase, nm
	Al	Ti	Zr	Cu			
12-1 as-cast	61.5	27.9	0	10.6	0.00	$L1_2$	0.394
	59.5	2.5	0	38.0	0.00		
12-1 homogenized	61.5	25.9	0	12.6	0.00	$L1_2$	0.395
	58.9	0.6	0	40.5	0.00		
12-2 as-cast	61.4	16.2	11.3	11.1	0.41	$L1_2$	0.400
	60.4	20.4	5.4	13.8	0.21	$L1_2$	0.397
	46.4	1.7	0.4	51.5	0.19		
12-2 homogenized	61.2	18.4	7.8	12.6	0.30	$L1_2$	0.397
	47.0	4.1	1.7	47.2	0.29		
12-3 as-cast	61.8	9.2	16.3	12.7	0.64	$L1_2$	0.403
	60.8	14.8	10.8	13.6	0.42	$L1_2$	0.398
	42.1	0.6	0.3	57.0	0.33		
12-3 homogenized	62.0	12.6	12.8	12.6	0.50	$L1_2$	0.400
	61.3	13.6	12.1	13.0	0.47	$L1_2$	0.400
	48.3	4.7	4.3	42.7	0.48		
12-4 as-cast	62.1	9.9	15.2	12.8	0.61	$L1_2$	0.403
	56.6	3.9	30.8	8.7	0.89		
	50.5	1.6	6.1	41.8	0.79		
12-4 homogenized	62.0	8.6	17.9	11.5	0.66	$L1_2$	0.403
	46.3	3.6	6.4	43.7	0.64		
12-5 as-cast	62.0	0	25.4	12.6	1.00	$L1_2$	0.407
	54.4	0	36.9	8.7	1.00		
	48.0	0	8.0	44.0	1.00		
	27.0	0	66.2	6.8	1.00		
12-5 homogenized	61.8	0	25.7	12.5	1.00	$L1_2$	0.406
	33.2	0	30.0	36.8	1.00		
	14.0	0	76.9	9.1	1.00		

The quaternary Al-Cu-Ti-Zr alloys will be discussed next. For the 8 alloy series, Table 6, when the Zr fraction varied from 0.21 to 1 only cubic $L1_2$ phases were found after homogenization. In alloys between Zr fractions of 0.5 and 0.67 two $L1_2$ phases were found. They contained different Zr fractions as well as somewhat different Al and Cu contents. Their lattice parameters are almost the same. The two distinct $L1_2$ phases are clearly shown in the SEM micrographs of alloy 8-3 as-cast and homogenized, Figure 12. The composition variation appears to result from dendritic growth, as the dendritic microstructure was still present after homogenization. While there may not be two cubic phases after full homogenization, the present results do suggest that the cubic phase field is quite large at 1000^{o}C. Voids formed during the homogenization anneal are also shown in Figure 12. Some of the voids from homogenization in other of the alloys were much larger. In the 12 series alloys two $L1_2$ phases are observed in alloy 12-3 with a Zr fraction of 0.5. The Cu compositions in the $L1_2$ phases in both series as cast varied over the range of 6.1 to 13.8 at. %. The range is less after homogenization, 6.7 to 12.6 at.% Cu. It is worth mentioning that previously two $L1_2$ phases were also observed in $Al_{66}Mn_9(Ti,Zr)_{25}$ intermetallic compounds[23]. Where the X-ray diffraction peaks were sufficiently distinct, the crystal structure of the phases could be identified as shown in Tables 6 and 7.

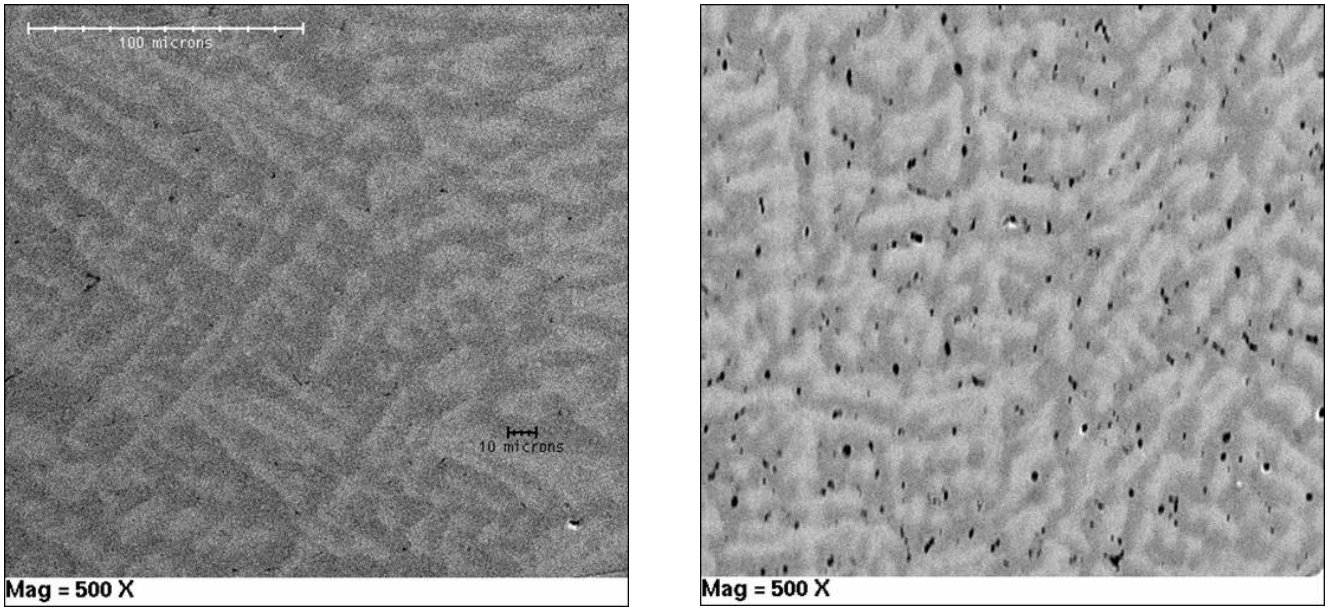

Figure 12. SEM micrograph of alloy 8-3: (a) as cast and (b) homogenized 72 hrs at 1000°.

The measured lattice parameters of the $L1_2$ phases as a function of Zr fraction are plotted in Figure 13. The measured values for the Zr only and Ti only $L1_2$ intermetallics are almost the same as those predicted from Figure 10. These experimental values are compared with the *ab initio* calculated values in Table 8. With the quarternary Al-Zr-Ti-Cu alloys the lattice parameter is almost a linear function of Zr fraction in the Cu containing alloys with the 0.404 nm value of Al being matched by a Zr/(Zr + Ti) fraction of 0.8. This is not very sensitive to the Cu fraction in the cubic alloys over the range observed. A quaternary Al-Cu-Zr-Ti alloy in this composition range appears to be a good candidate for forming a nanoscale coherent precipitate in an Al-matrix alloy.

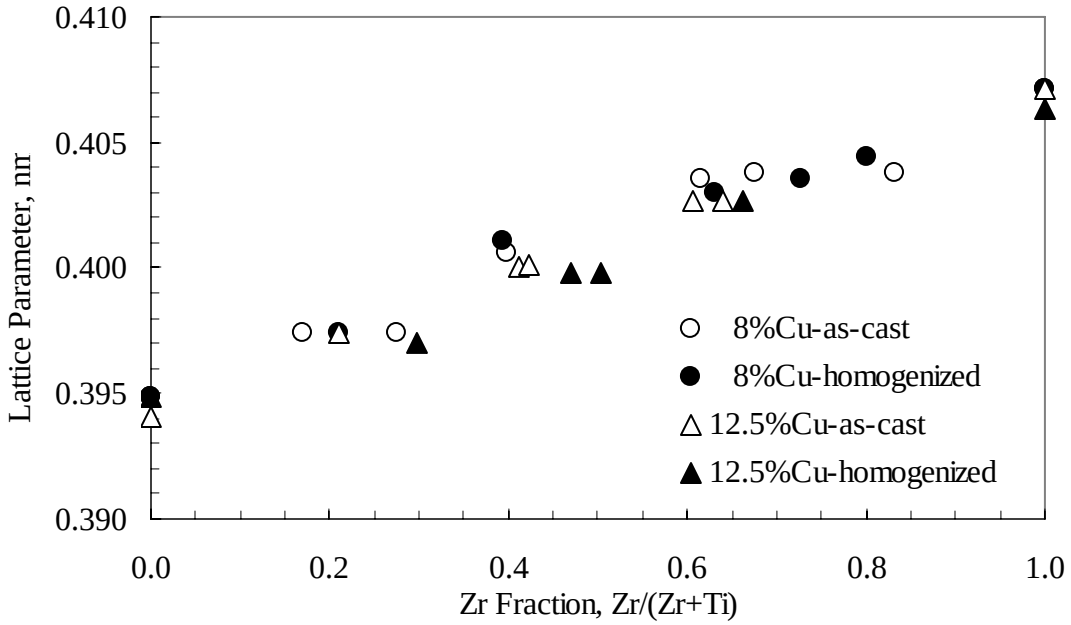

Figure 13. Measured lattice parameter of $L1_2$ phases as a function of Zr fraction in quaternary alloys containing copper.

The apparent densities of the alloys, plotted in Figure 14, increased approximately linearly with Zr fraction and except for two cases the values were little changed on homogenization, indicating that the volume fractions of voids are quite small. In the two cases where there was a significant difference, the homogenized sample had the highest density showing that the change is due to a change in the combinations of intermetallic compounds and their volume fractions. For example in alloy 8-5 where the Zr fraction relative to Ti is 1, the as-melted sample contains 3 phases but after homogenization only the $L1_2$ phase is present. The increase in density is about 2 %.

The measured values of Y, μ and B are given in Figure 15. The *ab initio* computed bulk moduli values for the 12 at.% Cu alloys of Al-Cu-Ti and Al-Cu-Zr alloys are compared with the measured values in Table 9. There is very little difference between the computed and measured values. As shown in Figure 15 the moduli of the $L1_2$ intermetallics change little by varying the Zr fraction from 0 to 1 as well as varying the Cu from 8 to 12.5 at %. Youngs modulus has the largest variation. It varies by 10 % with changing Zr fraction. The lowest Youngs modulus values obtained for the homogenized samples are for a Zr fraction of 0.5.

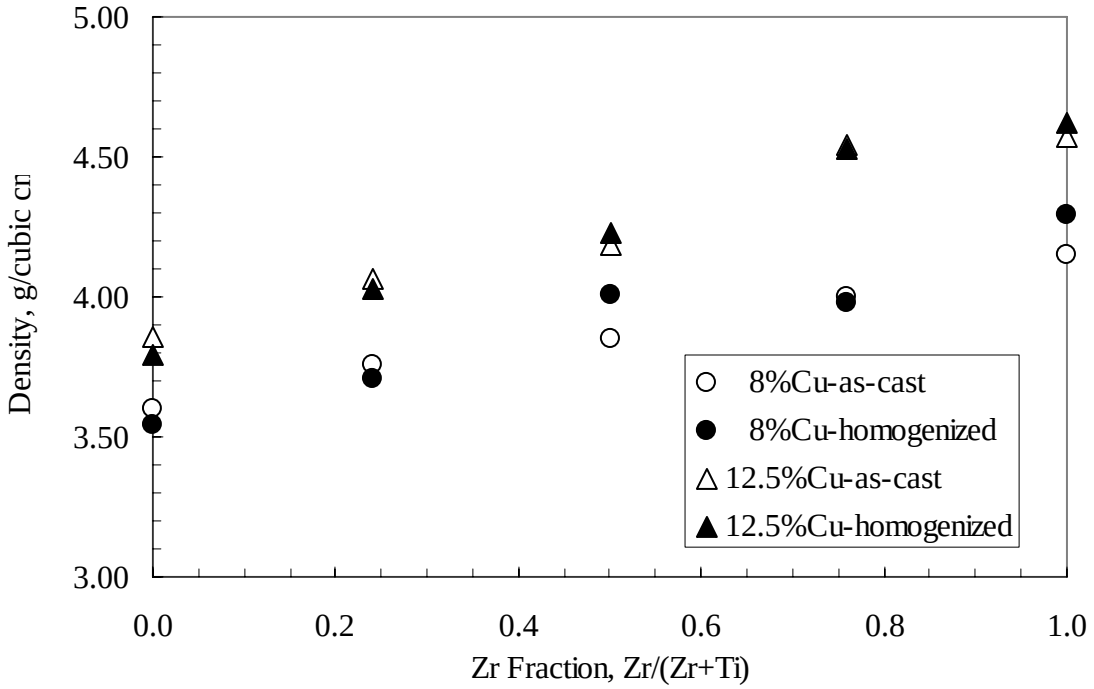

Figure 14. Measured densities of intermetallics as a function of Zr fraction.

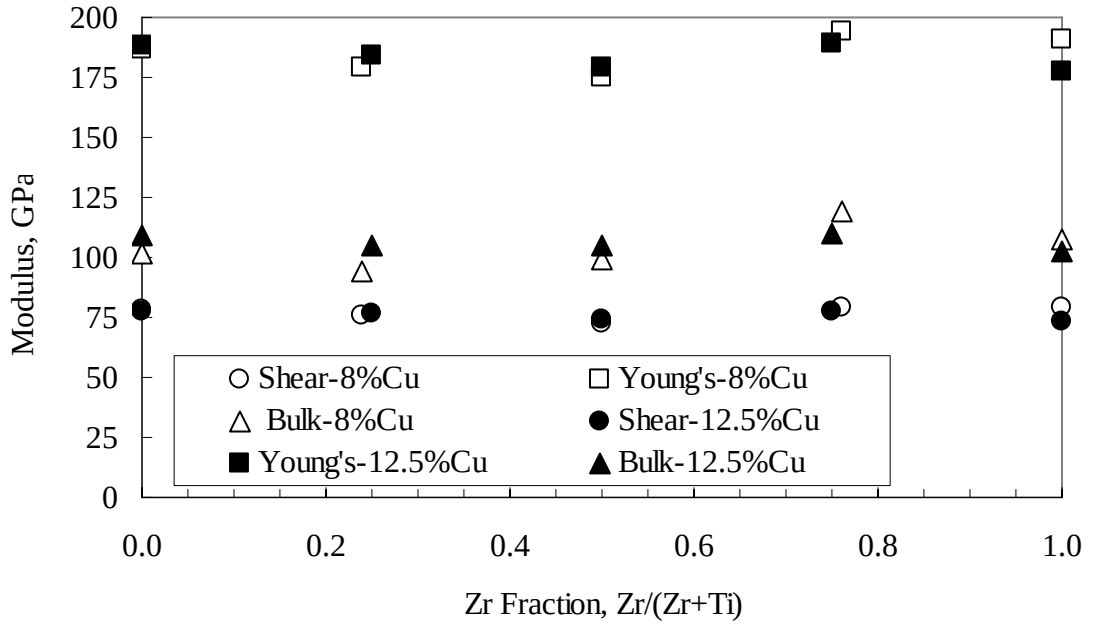

Figure 15. Measured shear, Young's and bulk modulus of homogenized intermetallics as a function of Zr fraction.

Table 8. Calculated (in Figure 11) and experimental values of bulk modulus (GPa) for homogenized ternary Al-Ti-Cu and Al-Zr-Cu alloys

	8 at.% Cu		12.5 at.%Cu	
	Calculated	Experimental	Calculated	Experimental
Al-Ti-Cu	105.5	102.2	107.0	108.8
Al-Zr-Cu	107.5	107.4	109.0	102.4

Experimental results obtained in the present work show that $(Al,Cu)_{0.75}Zr_{0.25}$ and $(Al,Cu)_{0.75}Ti_{0.25}$ intermetallics at 1000°C (the homogenization temperature employed in this work) display a relatively extensive phase field. The observed effect of Cu additions to stabilize the cubic $L1_2$ structure, relative to the tetragonal $D0_{22}$ and $D0_{23}$ structures observed in binary trialuminides, is consistent with the present ab-initio calculations. In the quaternary alloys, $L1_2$ phases were found with Cu content varying from 6.7 to 12.6 at % Cu. Interestingly, near the Zr/(Ti + Zr) fraction of 0.5, two $L1_2$ phases were observed in the microstructure as cast, as well as after homogenization at 1000°C. These two $L1_2$ phases differed in their measured Zr fraction. It is not certain whether this observation reflects an equilibrium two-phase coexistence, or whether it reflects composition variations arising from the dendritic cast structure that was not removed by the homogenization anneal.

The *ab-initio* calculated lattice parameters for the $L1_2$ phase at absolute zero agreed very well with measured values at room temperature for $Al_{0.63}$ $Cu_{0.12}$ $Zr_{0.25}$ and $Al_{0.67}$ $Cu_{0.12}$ $Ti_{0.25}$. The computed lattice parameter for the ternary Al-Ti-Zr alloys matched the lattice parameter of Al at approximately equal Ti and Zr fractions. Similar behavior was experimentally found in the quaternary $L1_2$ $(Al, Cu)_{0.75}$ $(Ti, Zr)_{0.25}$ intermetallics. The lattice parameter match with Al occurs at Zr/(Zr + Ti) of approximately 0.75 with Cu in the range of 8 to 12 at %. This is a target composition for precipitates in precipitation-strengthened creep resistance high temperature Al-base alloys.

With the elastic moduli there is again good agreement between the measured values and the calculated values for the ternary Al-Cu-Ti and Al-Cu-Zr $L1_2$ intermetallics. In the quaternary $L1_2$ $(Al, Cu)_{0.75}$ $(Ti, Zr)_{0.25}$ intermetallics there was surprisingly little variation in the measured elastic moduli with Zr fraction.

Overall, the comparisons between experiment and theory research facilitated by this research demonstrates high accuracy in the *ab initio* computation of phase stability, lattice parameters and elastic constants for the multicomponent trialuminide intermetallics considered.

3. Studies on Al-Zr and Al-Zr-Ti Alloys – Keith Knipling and Dieter Isheim

Introduction

Precipitation of cubic $L1_2$ structured Al-Zr and Al-Zr-Ti in an Al alloy matrix was investigated by local electrode atom probe (LEAP) tomography and transmission electron microscopy. Finally the creep properties were determined. The alloys were made by arc melting and solidified in the water cooled copper hearth. Aging was done without further solution treatment.

3.1 Composition of $Al_3(Zr_{1-x}Ti_x)$ precipitates at 375 and 425°C

Atom-probe tomography was utilized to verify directly the chemical composition of $Al_3(Zr_{1-x}Ti_x)$ ($L1_2$ structure) precipitates formed in Al-0.1Zr-0.1Ti (at.%) alloys during extended aging at 375 or 425°C. At 375°C the Zr/Ti ratio in the precipitates is 10, corresponding to precipitates of composition of $Al_3(Zr_{0.91}Ti_{0.09})$. At 425°C the precipitates contain approximately twice this amount of Ti, with precipitates of composition $Al_3(Zr_{0.83}Ti_{0.17})$. At both temperatures, the slower-diffusing Ti atoms are a minor constituent in the $Al_3(Zr_{1-x}Ti_x)$ phase although thermodynamics is also playing a role.

3.1.1 Precipitate compositions after extended aging at 425°C

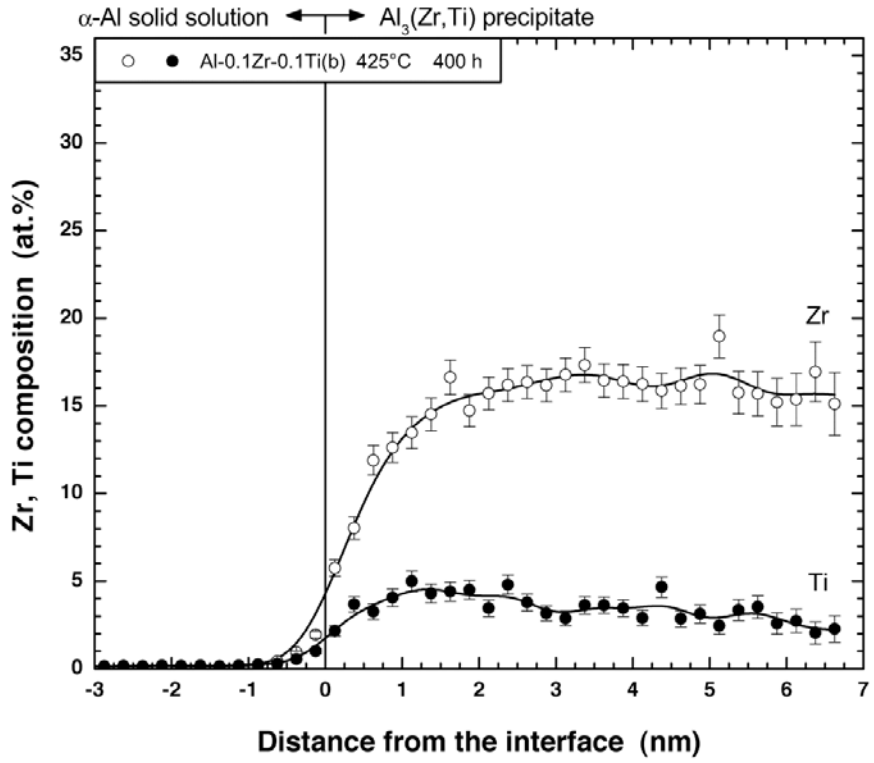

Figure 16: Proxigram displaying the distribution of Zr and Ti atoms relative to the position of a 5 at.% Zr isoconcentration surface. As exhibited, the precipitate is Zr-rich, with a small fraction of the Zr lattice sites replaced by Ti atoms. The ratio of Zr:Ti is about 5.

Figure 16 exhibits a proximity histogram, or proxigram for short [62], showing quantitatively the composition of an $Al_3(Zr_{1-x}Ti_x)$ precipitate formed after 400 h at 425°C. The proxigram in Figure 16 is sub-stoichiometric compared to that expected for a trialuminide (Al_3M-type) ordered phase. Ti is a minor constituent in the $Al_3(Zr_{1-x}Ti_x)$ precipitate, with an average Zr/Ti ratio of 5 (corresponding to x = 0.17) within the precipitate. This is much higher than the overall Zr/Ti ratio of unity in the alloy.

3.1.2 Temporal evolution of $Al_3(Zr_{1-x}Ti_x)$ precipitate compositions at 375°C

Figure 17 shows proxigrams for precipitates formed in Al-0.1Zr-0.1Ti (a) aged for 20, 400, or 1600 h at 375 °C. Compared to Figure 16, these concentration profiles are closer to stoichiometry (25 at. % total solute) and, as with 425°C aging temperature Ti is clearly a minor constituent in the $Al_3(Zr_{1-x}Ti_x)$ phase precipitated at 375°C. After 20 h at 375°C, the concentration of Ti in the precipitate is 3–4 at.%, comparable to that displayed in Figure 16 for Al-0.1Zr-0.1Ti(b) aged 400 h at 425°C. The Ti content of the precipitates varies little with aging time, 20–1600 h; however, the Zr content decreases a little on increasing the aging time from 20 to 400 hr.

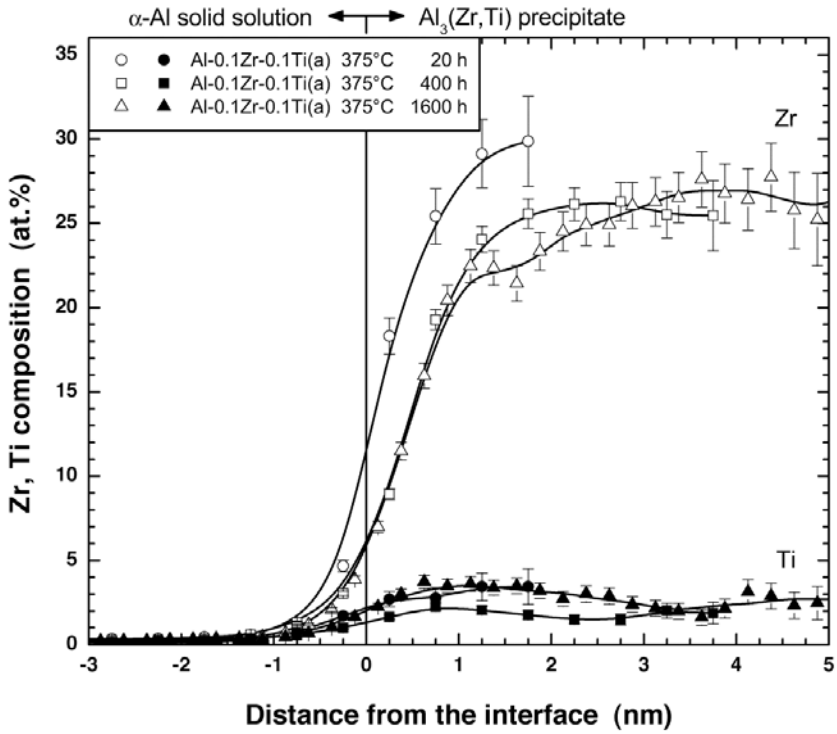

Figure 17: Proxigrams displaying the distribution of Zr and Ti atoms in $Al_3(Zr_{1-x}Ti_x)$ precipitates formed in Alloy Al-0.1Zr-0.1Ti(a) aged at 375°C for the times indicated. The 20 h aging time results are based on four precipitates and a total of 4.96×10^5 atoms, the results for 400 h are based on ten precipitates and a total of 9.09×10^5 atoms, and the results for 1600 h are based on four precipitates and a total of 3.07¥10^6 atoms.

3.2 Microstructure of Al alloy with $L1_2$ Al_3Zr and $Al_3(Zr_{1-x}Ti_x)$ precipitates: 425°C aging

3.2.1 TEM micrographs

Figures 18 and 19 show the microstructure of Al-0.1Zr(b) and Al-0.1Zr-0.1Ti(b) aged at 425°C for 1600 h. As observed by others [63-67], the nanoscale precipitates are inhomogeneously distributed due to segregation of Zr (and Ti) during dendritic solidification of the alloys. Associated with this dendritic precipitate distribution is a concomitant non-uniform distribution of precipitate morphologies, shown most clearly in Figure 19(a), in which very small (ca. 10 nm) coherent $L1_2$ precipitates, intermediate sized (ca. 20 nm) coherent and semicoherent $L1_2$ precipitates, and large plate-like precipitates are seen to coexist.

3.2.2 Precipitate size analyses

The most prevalent precipitate morphology is the fine population of coherent and homogeneously-distributed $L1_2$ precipitates found in the precipitate-rich dendritic regions (Figures 18(d) and 19(d)). According to these micrographs the coarsening resistance of the Al_3Zr precipitates is about the same as that of the $Al_3(Zr_{1-x}Ti_x)$ precipitates at 425°C the mean radius, $\langle R\rangle$, of Al_3Zr is 10.9 nm and that of $Al_3(Zr_{1-x}Ti_x)$ is 11.6 nm. Table 9 summarizes results of precipitate size analyses on more concentrated Al-0.2Zr and Al-0.2Zr-0.2Ti (at.%) alloys, which again indicate that coarsening rates of Al_3Zr and $Al_3(Zr_{1-x}Ti_x)$ precipitates are about the same after extended aging at 425°C.

Table 9: Mean precipitate radii, <*R*>, observed in the dendrite centers from six different Al-Zr and Al-Zr-Ti (three of each) specimens after extended aging at 425°C.

Alloy	Aging treatment	Mean precipitate radius, <*R*> (nm)	Number of precipitates counted
Al-0.1Zr(b)	1600 h at 425°C	10.9	251
Al-0.1Zr-0.1Ti(b)	1600 h at 425°C	11.6	143
Al-0.2Zr(a)	400 h at 425°C	5.1	300
		6.7	310
Al-0.2Zr-0.2Ti(a)	400 h at 425°C	6.3	101
		5.9	117

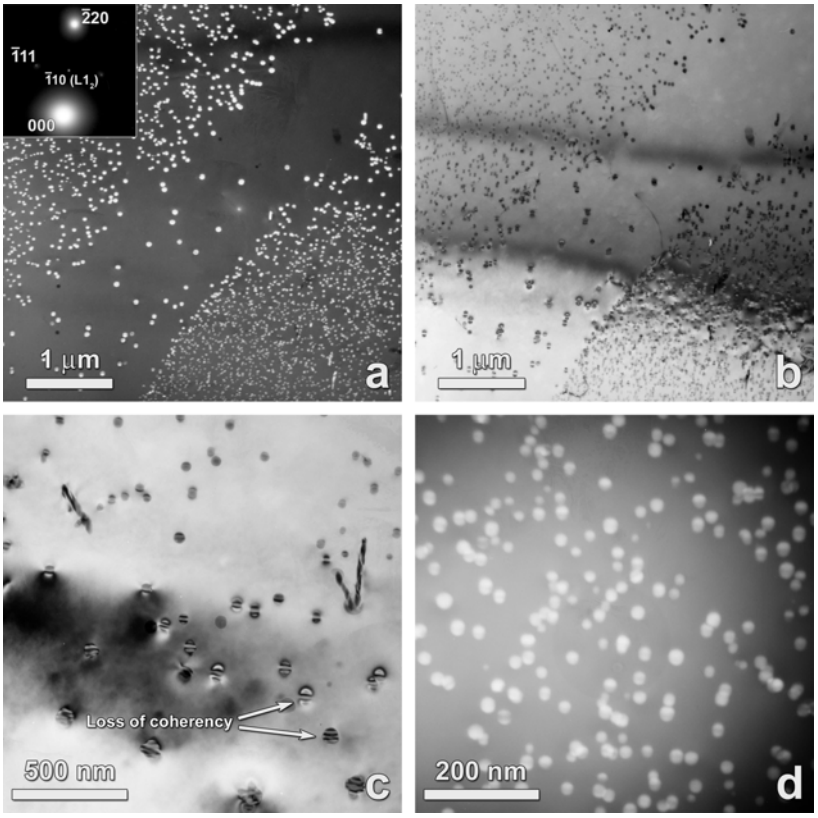

Figure 18: TEM micrographs of alloy AZ-1b aged 1600 h at 425°C. All images obtained under dynamical two-beam conditions, the specimen oriented near the [110] zone axis with $\vec{g} = (\bar{2}20)$ operating. Dark field micrographs were imaged with the $(\bar{1}10)$ $L1_2$ superlattice reflection as indicated in the inset diffraction pattern. (a) Dark field micrograph showing a 1.5 m-wide interdendritic channel separating two precipitate-rich dendritic regions. (b) Corresponding bright field micrograph to the image in panel a. All precipitates in this micrograph — including the relatively coarse (35 nm radius) interdendritic ones — exhibit classic Ashby-Brown strain contrast indicative of precipitate coherency with the Al matrix. (c) Bright field micrograph showing showing strain contrast from larger precipitates in an interdendritic region. There is a gradient in precipitate size (associated with an initial inhomogeneous distribution of solute), with a similar variation in strain contrast. In this image the precipitates range in size from <*R*> = 25–50 nm, with the smaller ones (<*R*> = 40 nm) exhibiting distinct Ashby-Brown strain contrast. (d) Centered dark field image of the fine, coherent, homogeneously-nucleated $L1_2$ Al_3Zr precipitates from within a dendrite center. The precipitates range in size from <*R*> = 4.7–15.1 nm, with a mean radius of <*R*> = 10.9 nm.

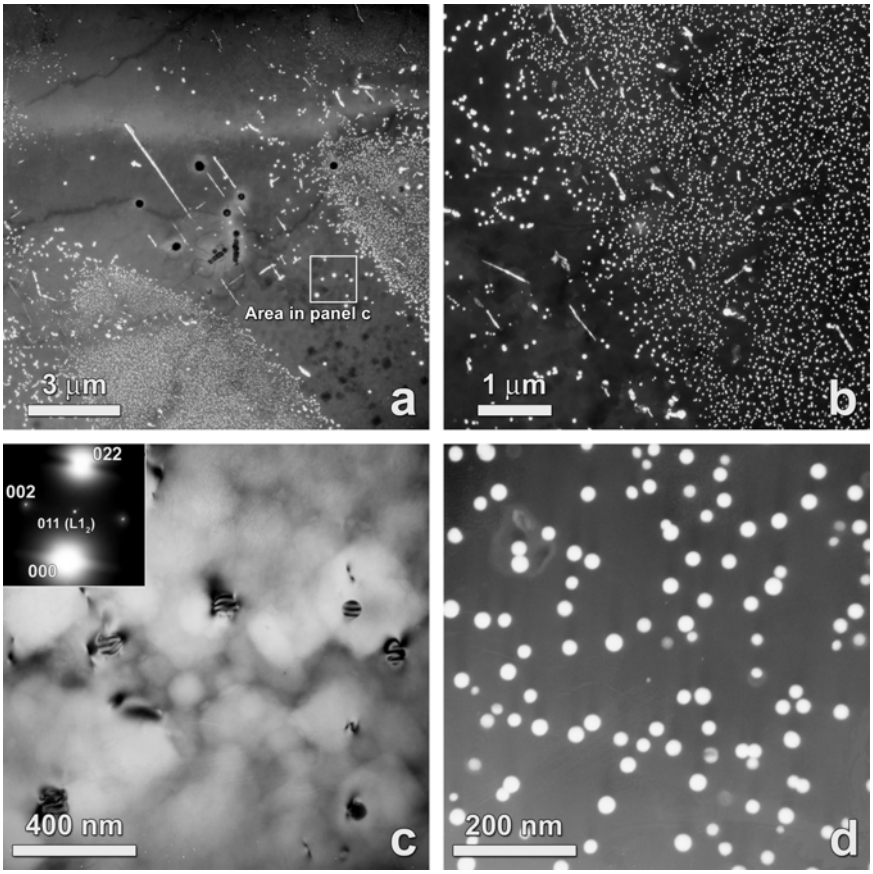

Figure 19: TEM micrographs of alloy AZT-1b aged 1600 h at 425°C. All images obtained under dynamical two-beam conditions, the specimen oriented near the [100] zone axis with $\vec{g}$=(022) operating. Dark field micrographs were imaged with the (011) $L1_2$ superlattice reflection as indicated in the inset diffraction pattern. (a) Relatively low magnification dark field image showing various precipitate morphologies associated with the initially inhomogenous distribution of solute. Precipitate-rich dendritic regions are separated by a 4–5 m wide precipitate-lean interdendritic band. Within the interdendritic (low solute) regions are large orthogonal rods or plates, up to 4 m in length, with a cube-on-cube orientation with the matrix. (b) Detail view of dendritic-interdendritic boundary. In the precipitate-rich dendritic region there is evidence of precipitate coalescence, as evidenced by linear arrays, 100–500 nm in length, of spherical $Al_3(Zr_{1-x}Ti_x)$ precipitates surrounded by precipitate-denuded regions extending ca. 80–250 nm radially around the coalesced arrays. (c) Bright field micrograph showing showing strain contrast from the relatively large (<*R*> = 40–60 nm) interdendritic precipitates (area indicated in panel a). Unlike the finer $Al_3(Zr_{1-x}Ti_x)$ precipitates found in the dendritic regions, these larger precipitates do not exhibit Ashby-Brown strain contrast and have therefore partially lost coherency with the Al matrix. (d) Centered dark field image of the fine, coherent, homogeneously-nucleated $L1_2$ $Al_3(Zr_{1-x}Ti_x)$ precipitates from within a dendrite center. The precipitates range in size from <*R*> = 3.7–15.6 nm, with a mean radius of <*R*> = 11.6 nm.

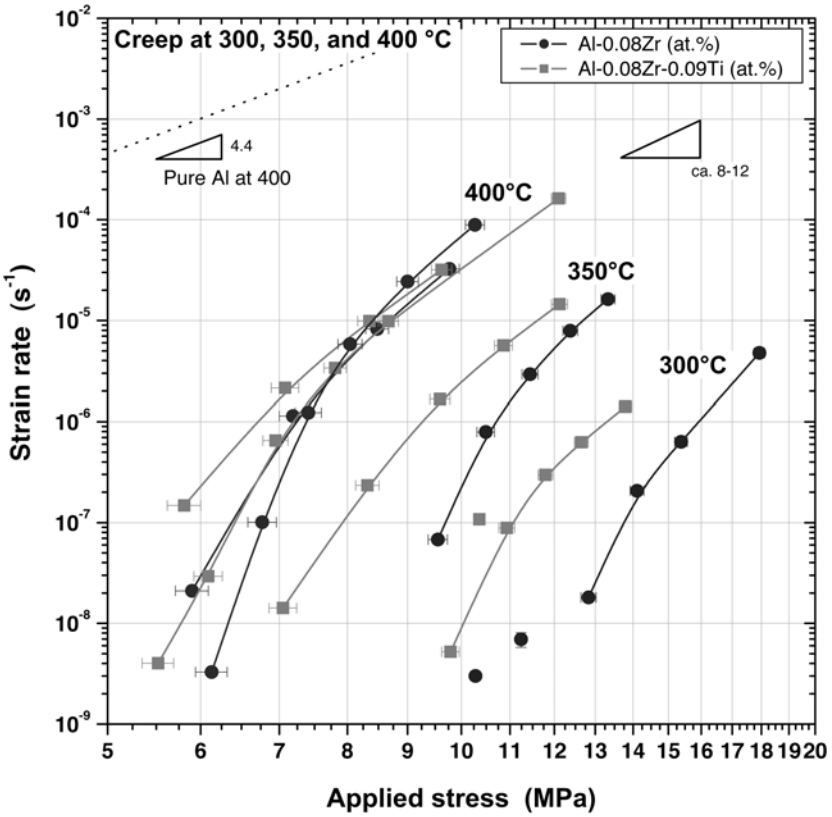

Figure 20: Double logarithmic plot of minimum creep rate at 300, 350, and 400°C vs. applied stress, for Al-0.1Zr and Al-0.1Zr-0.1Ti alloys aged for 100 h at 400°C.

3.3 Creep results

Creep results for the Al-0.1Zr and Al-0.1Zr-0.1Ti (at.%) alloys, performed at 300, 350, and 400°C, are shown in Figure 20. Despite the non-uniform precipitate distribution and the associated precipitate-free interdendritic channels, the Al-Zr and Al-Zr-Ti alloys show moderate creep resistance at 300–400°C. The apparent stress exponent, n = 8–12, of both alloys is much higher than for pure Al (n = 4.4), indicative of the existence of a threshold stress. Extrapolating the low strain rate data at 300°C for each alloy to $\varepsilon = 10^{-10}$ s^{-1} suggests that this threshold stress is 10–12 MPa for the binary Al-Zr alloy and 9–10 MPa for the ternary Al-Zr-Ti alloy. The threshold stress and creep rates at 300° C are comparable to those observed in previous creep studies on the more expensive Al-Sc alloys at 300°C [68- 70] but there is no data for higher temperatures for the latter.

At 300, 350, and 400°C, the ternary Al-Zr-Ti alloy is somewhat poorer in creep resistance than the binary Al-Zr alloy. This may be attributable to two independent phenomena: (i) a smaller grain size in the ternary Al-Zr-Ti alloy as determined by macro-examination of the ingots and (ii) reduction in the lattice parameter mismatch of $Al_3(Zr_{1-x}Ti_x)$ with α-Al.

3.4 Summary

Aluminum with cubic $L1_2$ structured precipitates of nominal composition Al_3 Zr or Al_3 (Zr,Ti) show promise for creep resistance at elevated temperatures even thought the cast structure is highly homogeneous due to the solidification process. The strengths of the alloys are too low so it is unlikely that these precipitates would be used alone but they are candidates for addition to an alloy with other reinforcement. This is the subject of the next section. Even though the cubic precipitates are metastable,

transformation to or precipitation of the stable tetragonal forms did not occur even up to 1600 hrs at 425° C, the longest time investigated. The coarsening rate of the cubic precipitates with aging is extremely low.

PART 4. Microstructure and Creep Properties of Castable Alloys Based on Al-Ni Eutectic– S. Vaynman and D. Isheim

Introduction

Alloys based on Al-Ni eutectic containing nano-scale $L1_2$ precipitates show promise as the basis for developing a castable high-temperature creep-resistant alloy. The Al_3Ti intermetallic phase that forms during eutectic solidification gives reinforcement to the alloy while the $L1_2$ precipitate strengthens the Al matrix. The age hardening experiments at 425˚C, the creep studies at 350˚C and microstructure investigations were focused on aluminum-nickel eutectic (Al-2.68 at. % Ni) and aluminum-nickel-eutectic based alloys with additions of Zr and Ti (Al-0.18 at.% Zr -2.72 at.% Ni and Al -0.12 at.% Zr-0.053 at.% Ti-2.72 at.% Ni). The alloys were made by arc melting and solidification in the water cooled Cu hearth. They were investigated without further treatment.

4.1 Mechanical Properties

Ambient temperature hardness measurements show a peak in hardness (with values up to 75 HV) after 72-100 hrs of aging at 425˚C. However, with prolonged aging the hardness of these alloys decreases most likely due to coarsening of the precipitates as well as the coarsening and spheroidization of the lamellar eutectic microstructure that was observed in microstructural observations.

A comparison of creep behavior at 350^{o}C of Al-Ni eutectic alloy and a eutectic alloy with 0.053 at.% Ti and 0.12 at.% Zr added, both aged for 72 hrs at 425^{o}C, is shown in Figure 21(a) where stress and strain rate are plotted on the double log basis. It is evident that addition of Zr and Ti to Al-Ni eutectic reduces the creep rate, especially at higher stresses. For comparison Figure 21 also includes 300^{o}C creep data for a nickel-free Al-2.1at.%Mg-0.16 at.% Sc alloy with precipitates of 5.6 nm diameter [60]. The present precipitates are approximately this size as presented below. The creep resistance of the Al-Ni-based eutectic alloys at 350^{o}C is about the same as that of Al-2wt.%Mg-0.2wt.% Sc alloy crept at 300^{o}C. The eutectic alloys are actually better at low stresses but the creep resistance of the Al –Mg-Sc alloy increases substantially as the precipitate size increases [60]. A more detailed comparison of secondary creep rate at 350^{o}C of the three eutectic-based alloys at 19 MPa stress is shown in Figure 21(b), which plots strain vs. time. The steady state creep rate of the binary Al-Ni eutectic alloy at 19 MPa stress is 3 X 10^{-8} sec^{-1}. Adding 0.18at% Zr reduces it to 1.4 X 10^{-8} sec^{-1} and with 0.053 at. % Ti and 0.120 at.% Zr thee creep rate is still lower, 0.725 X 10^{-8} sec^{-1}. These results show that combined precipitation and reinforcement is indeed a viable approach for developing a high temperature creep resistant Al base alloy. The results for the Al-Mg-Sc alloy [60] suggest that the creep resistance could be increased substantially in the Al-Ni-Zr-Ti by increasing the precipitate size.

4.2 Atom Probe Tomography

The composition, morphology and size of the nano-scale $Al_3(Zr,Ti)$ precipitates were studied in detail by linear electrode atom-probe (LEAP) tomography in two alloys, one with a small amount of Ni, Al-0.12 Zr-0.053 Ti-0.045 Ni (at.%) and the other with the eutectic ratio of Al to Ni, Al-0.12 Zr-0.053 Ti-2.72 Ni (at.%). Both alloys were aged at 425^{o}C for 24h. A three-dimensional atom-by-atom reconstruction of a volume of the hypoeutectic Al to Ni ratio alloy is displayed in Figure 22(a). These experiments confirm the presence $Al_3(Zr,Ti)$ precipitates that are about 6 nm in diameter.

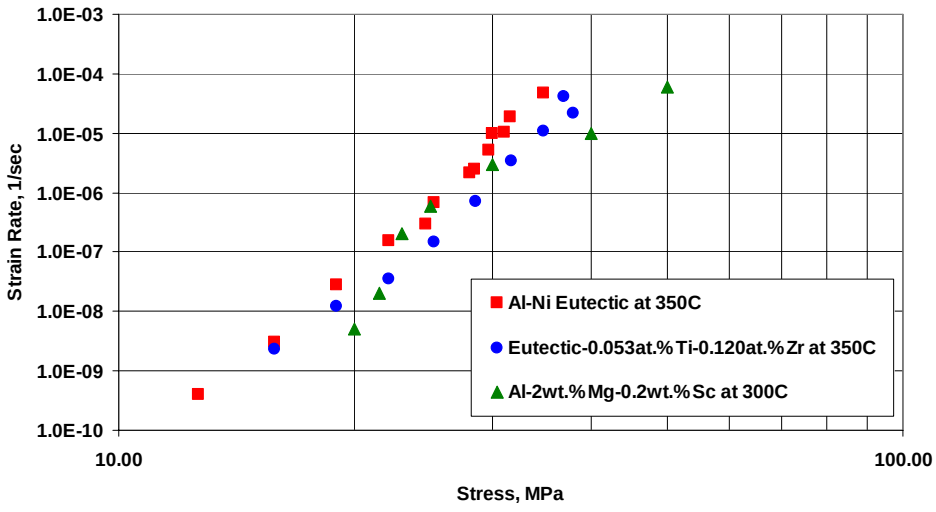

a

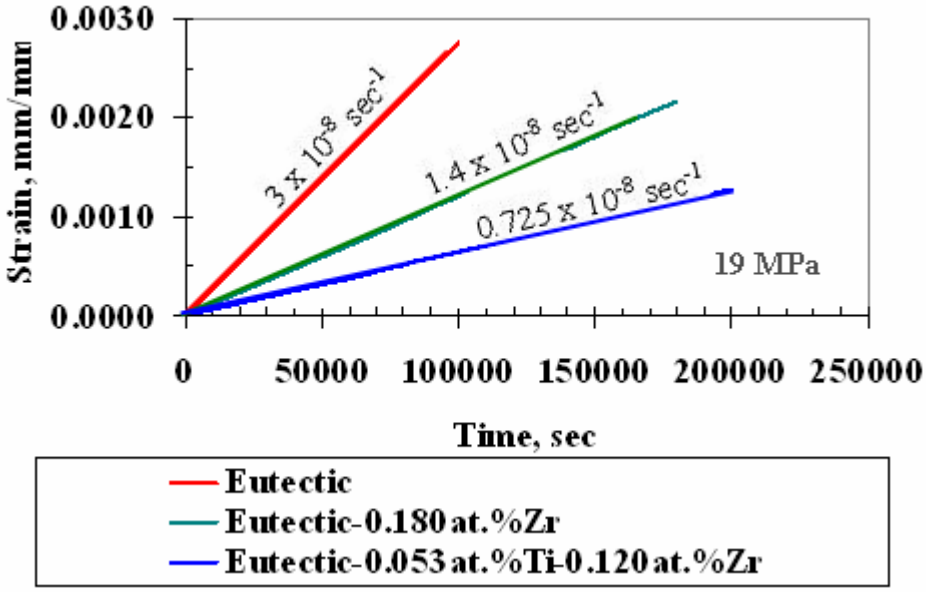

b

Figure 21. (a) Steady state creep rate at 350°C of Al-Ni eutectic and Al-Ni-based eutectic with 0.053 at.% Ti and 0.120 at.% Zr alloys. Prior to creep tests both alloys were aged for 72 hrs at 425°C. Also included is the creep rate at 300°C of Al-2.1at.% Mg-0.16 at.% Sc alloy with approximately the same precipitate diameter, 5.6 nm [60] In this alloy the threshold stress increased substantially as the precipitate radius increased reaching a maximum of 27 MPa at approximately 12 nm. (b) Steady creep of Al-Ni eutectic and eutectic alloys that contain Zr and Ti at 350°C under the stress of 19 MPa. Prior to creep tests alloys were aged for 72 hrs at 425°C. The steady state creep rates at 19 MPa stress were 3 X 10^{-8} sec^{-1}, 1.4 X 10^{-8} sec^{-1} and 0.725 X 10^{-8} sec^{-1} respectively.

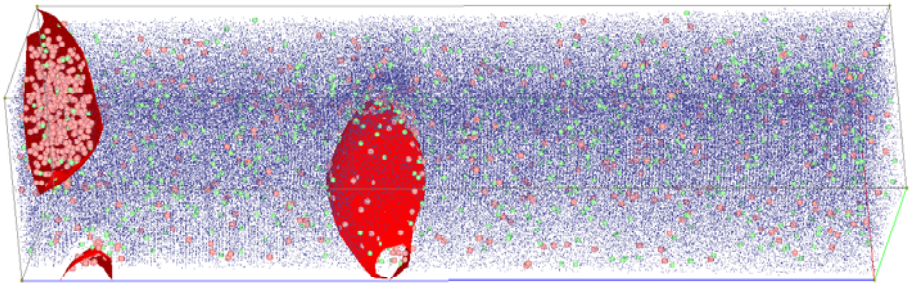

a

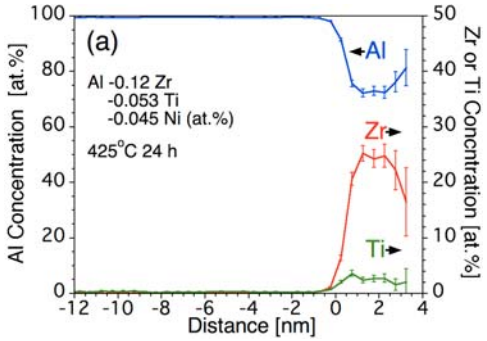

b

Figure 22. (a) 3D reconstruction of $Al_3(Zr,Ti)$ precipitates in Al-0.12 Zr-0.053 Ti-0.045Ni (at.%), aged at 425°C for 24 h. Al atoms are shown in blue, Zr in red, and Ti in green. The superposed isoconcentration surfaces at the 5 at.% Zr level, in red, delineate the precipitates. The reconstruction contains 243,251 atoms in a volume 12 x 12 x 51 nm^3. (b) Proximity histogram concentration profile with respect to a 5 at.% Zr isoconcentration interface in an Al-0.12 Zr-0.053 Ti-0.045Ni (at.%) alloy.

A compositional analysis of the precipitates in the 3D reconstruction of an Al-0.12 Zr-0.053 Ti-0.045Ni (at.%) alloy is obtained by the proximity histogram method, (proxigram for short), which produces a concentration profile with respect to distance from an isoconcentration surface, is shown in Figure 16(b). The precipitates are represented at positive distances at the right-hand side of the diagrams; the origin is the position of the isoconcentration surface, and concentrations at negative distances represent the Al-rich matrix. The precipitate compositions in two alloys can be summarized as follows: The Zr contents are 24.6 ± 0.9 and 26.4 ± 0.5 at.%, in the hypo-eutectic and the eutectic alloy, respectively, the Ti contents are 2.5 ± 0.3 or 0.6 ± 0.1 at.%, respectively, but no Ni within the error limits given by counting statistics. The small Ti content of the precipitates is possibly due to the significant solubility of Ti in Al_3Ni of about 1 at. % at 600°C [71] that leads to a reduction of the amount of Ti left for the formation of $Al_3(Zr,Ti)$ precipitates. The decrease in Ti in the precipitate with increase in Ni content and fraction of Al_3Ni is evidence for this suggestion. The absence of Ni in the cubic precipitates means that the Ni partitions almost completely to the Al_3Ni phase although kinetics may play a role.

Since the Ti largely partitions to the Al_3Ni phase rather than the Al_3 (Zr, Ti) phase, its low diffusivity may reduce diffusional creep in Al_3Ni phase thereby reducing the creep rate.

Final Comments

The two most important findings of this research are:

1. Computationally designing and then experimentally producing an alloy with thermodynamically stable cubic $L1_2$ $(Al,Zn)_3Zr$ precipitates that form on aging in an Al alloy matrix. This could be the basis for developing a new class of Al alloys.
2. Demonstrating that combined reinforcement and precipitation strengthening is a method for developing a high temperature creep resistant Al base alloy. Zirconium and titanium were added to eutectic Al-Ni alloy. The intermetallic Al_3Ni that formed during eutectic solidification was the reinforcing phase. The matrix was strengthened by cubic $L1_2$ precipitates. These precipitates were Al_3Zr with a small amount of Ti substituting for the Zr. Low creep rate at 350° C was found. Even though these precipitates are metastable, extensive LEAP tomography and TEM showed no evidence for transformation to the stable phase even after many hundreds of hours at 425° C; however, the eventual goal of the research was to further develop the Al alloy matrix and $(Al,Zn)_3Zr$ precipitate system to use it instead.

References

1. M.E. Fine, G. Ghosh, D. Isheim, S. Vaynman, J. Weertman, Alloy design of nanoscale precipitation strengthened alloys: Design of a heat treatable aluminum alloy useful to 400°C, Proposal to DOE Feb. 2002.
2. A. Raman and K. Schubert, Z. Metallkde, **56,** 40-43, 99-104 (1965).
3. V.R. Parameswaran, J.R. Weertman, and M.E. Fine, *Scripta Met.* **23,** pp. 147-150 (1989).
4. C.H. Tsau and Y.C. Chen, *Mater. Chem. Phys.* **73**, 111-117 (2002).
5. H. Ohmura, M.E. Fine, and T. Miyoshi, U.S. Patent No. 4,906,531, Mar. 6, 1990.
6. N.A. Belov, A.N. Alabin, and D.G. Elkin, *Scripta Mat.* **50,** 89 – 94 (2004).
7. G. Kresse and J. Furthmuller, "Efficient iterative schemes for ab initio total-energy calculations using a plane-wave basis set," *Phys. Rev*., **B 54**, 11169-11186 (1996).
8. G. Kresse and J. Furthmuller, "Efficiency of ab-initio total energy calculations for metals and semiconductors using a plane-wave basis set," *Computational Materials Science*, **6**, 15-50 (1996).
9. G. Kresse and J. Hafner, "Ab initio molecular-dynamics for liquid-metals," *Phys. Rev*., **B 47**, 558-561 (1993).
10. D. Vanderbilt, "Soft self-consistent pseudopotentials in a generalized eigenvalue formalism," *Phys. Rev*., **B 41**, 7892-7895 (1990).
11. Y. Nakayama and H. Mabuchi, "Formation of ternary $L1_2$ compounds in Al_3Ti-base alloys," *Intermetallics*, **1**, 41-48 (1993).
12. A. Raman and Schubert, "On the constitution of some alloy series related to $TiAl_3$. I Investigations in some T^4-Zn-Al-, T^4-Zn-Ga- and T^4-Ga-Ge Systems," *Z. Metallkde*., **56**, 40-43 (1965).
13. G. Ghosh and M. Asta, "First-principles calculation of structural energetics of Al-TM (TM=Ti,Hf,Zr) intermetallics," *Acta Materialia,* **53**, 3225-3252 (2005).
14. G. Ghosh, A. van de Walle, and M. Asta, "First-principles phase stability calculations of $L1_2$, DO_{22} and DO_{23} structures in Al-TM(=Ti,Zr,Hf) systems," *Proc. Int. Conf. Solid-Solid Phase Transformations in Inorganic Materials 2005 (PTM'05)*, Edited by J.M. Howe, D.E. Laughlin, J.K. Lee, U. Dahmen, and W.A. Soffa, TMS, Warrendale, PA, **Vol. 2**, 651-656, 2005.
15. V. Ozolins and M. Asta, "Large Vibrational Effects upon calculated phase boundary in Al-Sc," *Phys. Rev. Lett*., **86**, 448-451 (2001).
16. C. Wolverton, and V. Ozolins, "Entropically favored ordering: The metallurgy of Al_2Cu revisited," *Phys. Rev. Lett.*, **86**, 5518-5521 (2001).

17. A. van de Walle and G. Ceder, "The effect of lattice vibrations on substitutional alloy thermodynamics," *Rev. Mod. Phys*., **74**, 11-45 (2002).
18. Z. Liu, Doctoral research in progress, Northwestern University, June 2006.
19. E.A. Marquis and D.N. Seidman, "Nanoscale structural evolution of Al_3Sc precipitates in Al(Sc) alloys," *Acta Mater*., **49**, 1909-1919 (2001).
20. M.S. Zedalis and M.E. Fine, "Precipitation and Oswald ripening in dilute Al base-Zr-V alloys," *Metall. Trans. A*, **17A**, 2187-2198 (1986).
21. V.R. Parameswaran, J.R. Weertman, and M.E. Fine, "Coarsening behavior of $L1_2$ phase in an Al-Zr-Ti alloy," *Scripta Metall.*, **23**, 147-150 (1989).
22. J. Royset and N. Ryum, *Int. Materials Reviews*, **50**, 19 (2005).
23. C.D. Turner, W.O. Powers, J.A. Wert, Acta Metall., **37,** 2635 (1989).
24. I.S. Virk, R.A. Varin, *Scripta Metall. Mater.*, **25,** 85 (1991).
25. I.S. Virk, R.A. Varin, *Scripta Metall. Mater.*, **25,** 1381 (1991).
26. S.Z. Han, B.S. Rho, H.M. Lee, S.K. Choi, *Intermetallics*, **4,** 245 (1996).
27. T. Takashi, et. al., *Mat. Sci. Eng.*, **A329-331,** 474 (2002).
28. I.S. Virk, R.A. Varin, *Metall. Trans.*, **23A,** 617 (1992).
29. U. Prakash, R.A. Buckley, H. Jones, and C.M. Sellars, *J. Mater. Sci.*, **27,** 2001 (1992).
30. A. Virdis, V. Zwicker, *Z. Metallkde.*, **62**, 46 (1971).
31. V. Ya. Markiv, V.V. Burnashova, and V.R. Ryabov, *Akad. Nauk Ukr. SSR Metall.*, **46**, 103 (1973).
32. J. Tarnacki and Y.W. Kim, *Scripta Metall.*, **22**, 329 (1988).
33. S. Mazdiyasni, D.B. Miracle, D.M. Dimiduk, M.G. Mendiratta, and P.R. Subramanian, *Scripta Metall.*, **23**, 327 (1989).
34. A.J. Maeland and D. Narimhan, *MRS Symp. Proc.*, **133,** 723 (1989).
35. Y. Nakayama and H. Mabuchi, *Intermetallics*, **1**, 41 (1993).
36. T. Hong and A.J. Freeman, *J. Mater. Res.*, **6**, 330 (1991).
37. J. P. Perdew, in *Electronic Structure of Solids '91*, edited by P. Ziesche and H. Eschrig, Academic Verlag, Berlin, 1991.
38. H.J. Monkhorst and J.D. Pack, *Phys. Rev.*, **13B**, 5188 (1976).
39. M. Methfessel, A.T. Paxton, *Phys. Rev.*, **40B,** 3616 (1989).
40. P. Vinet, J.H. Rose, J. Ferrante, and J.R. Smith, *J. Phys.: Condens. Matter.*, **1**, 1941 (1989).
41. M.J. Mehl, B.M. Klein, and K. Papaconstatopolous, in Intermetallic Compounds: Vol. 1, Principles, edited by J.H. Westbrook and R.L. Fleischer, John Wiley & Sons, NY, (1994) 195.
42. W. Voigt, Lehrbuch der Kristallphysik, Teubner, Leipzig, Germany, 1928.
43. A.Z. Reuss, *Angew. Math. Phys.*, **9**, 49 (1929).
44. R. Hill, *Proc. Phys. Soc. Lond.*, **A65**, 349 (1952).
45. A.V. Hershey, *J. Appl. Mech.*, **21**, 236 (1954).
46. E. Kröner, *Z. Phys.*, **151**, 504 (1958).
47. C. Amador, J.J. Hoyt, B.C. Chakoumakos, and D. de Fontaine, *Phys. Rev. Lett.*, **74**, 4955 (1998).
48. C. Colinet, A. Pasturel, *Intermetallics*, **10**, 751 (2002).
49. S. Srinivasan, P.B. Desch, and R.B. Schwarz, *Scripta Metall. Mater.*, **25**, 2513 (1991).
50. T. Klassen, M. Oehring, and R. Bormann, *Acta Mater.*, **45**, 3935 (1997).
51. Z. Lauer St Gual, H. Wolf, and Th. Wichert, *Mater. Sci. Forum*, **269**, 485 (1998).
52. M. Alatolo, M. Weinert, and R.E. Watson, *Phys. Rev.*, **57B**, R2009 (1998).
53. C. Colinet and A. Pasturel, *J. Alloys and Compounds*, **319**, 154 (2001).
54. D. de Fontaine, *Solid State Physics*, **47**, 33 (1994).
55. C.L. Fu, *J. Mater. Res.*, **5**, 971 (1990).

56. M.H. Yoo, C.L. Fu, *ISIJ International*, **31**, 1049 (1991).
57. E. Clouet, J.M. Sanchez, and C. Sigli, *Phys. Rev.*, **65B**, 94105 (2002).
58. M. Nakamura and K.J. Kimura, *Mater. Sci.*, **26**, 2208 (1991).
59. G. Ghosh and G.B. Olson, *Acta Mater.*, **50**, 2655 (2002).
60. E.A. Maruis, D.N. Seidman, and D.C. Dunand, *Acta Mater.*, **51**, 4751 (2003).
61. O.C. Hellman and D.N. Seidman, *Microscopic Microanalysis*, **6**, 437 (2000).
62. O.C. Hellman and D.N. Seidman, *Mater. Sci. Eng. A*, **327**, 24 (2002).
63. N. Ryum, *Acta Metall*. **17** (1969).
64. O. Izumi and D. Oelschlagel, *Scripta Metall.*, **3**, 619 (1969).
65. O. Izumi and D. Oelschlagel, *Z. Metallk.*, **60**, 845 (1969).
66. E. Nes., *Acta Metall.* **20**, 499 (1972).
67. S. Hori, *J. Japan Inst Light Metals*, **27**, 129 (1977).
68. M.E. Van Dalen, D.C. Dunand, and D.N. Seidman, *Acta Mater.*, **53**, 4225 (2005).
69. C.B. Fuller, D.N. Seidman, and D.C. Dunand, *Acta Mater.*, **50**, 691 (2002).
70. D.N. Seidman, E.A. Marquis, and D.C. Dunand, *Acta Mater.*, **50**, 4021 (2002).
71. P. Villars, A. Prince, H. Okamoto, Eds. Handbook of Ternary alloy Phase Diagrams, Vol. 4 ASM International, 4212 (1995).